

Dynamic response of submarine obstacles to two-phase landslide and tsunami impact on reservoirs

**Jeevan Kafle, Parameshwari Kattel,
Martin Mergili, Jan-Thomas Fischer &
Shiva P. Pudasaini**

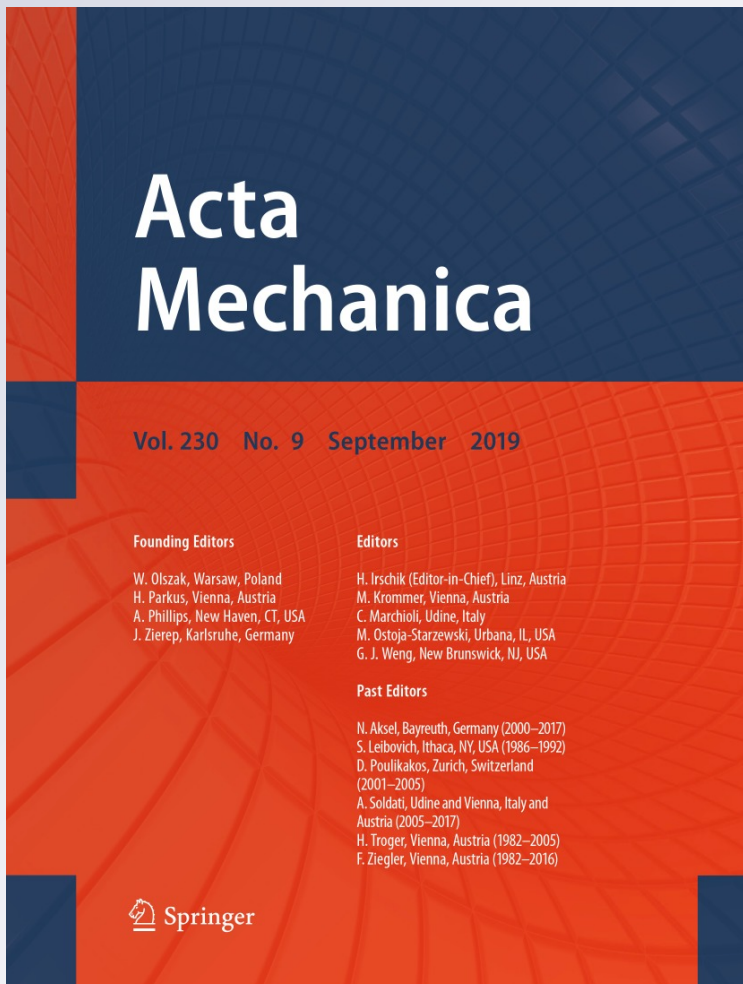
Acta Mechanica

ISSN 0001-5970

Volume 230

Number 9

Acta Mech (2019) 230:3143–3169
DOI 10.1007/s00707-019-02457-0



Your article is protected by copyright and all rights are held exclusively by Springer-Verlag GmbH Austria, part of Springer Nature. This e-offprint is for personal use only and shall not be self-archived in electronic repositories. If you wish to self-archive your article, please use the accepted manuscript version for posting on your own website. You may further deposit the accepted manuscript version in any repository, provided it is only made publicly available 12 months after official publication or later and provided acknowledgement is given to the original source of publication and a link is inserted to the published article on Springer's website. The link must be accompanied by the following text: "The final publication is available at link.springer.com".

**ORIGINAL PAPER**

Jeevan Kafle · Parameshwari Kattel · Martin Mergili ·
Jan-Thomas Fischer · Shiva P. Pudasaini

Dynamic response of submarine obstacles to two-phase landslide and tsunami impact on reservoirs

Received: 6 December 2018 / Revised: 30 April 2019 / Published online: 2 July 2019
© Springer-Verlag GmbH Austria, part of Springer Nature 2019

Abstract Submarine landslides may generate super-tsunamis as they interact with water bodies such as oceans, mountain lakes or reservoirs. These water bodies may contain solid objects (obstacles), which substantially alter the mass flow dynamics and reduce the devastating effects of submarine landslide and tsunami. Submarine landslides, the related tsunamis, and their interactions with obstacles are more complex than subaerial landslides and their obstacle-interactions. In order to mitigate mountain and coastal hazards and maintain the integrity of a hydraulic reservoir, it is important to properly understand submarine landslide and tsunami interactions with obstacles. Existing approaches cannot take into account other important aspects of interfacial momentum transfer in mixture flows such as interfacial drag, buoyancy, mobility of the fluid at the particle surface, and virtual mass force, which play important roles in the more accurate prediction of mixture flow dynamics by dynamic interactions between the landslide mass and the water. In order to include these important physics of two-phase mass flows and especially to include dynamic interactions between the landslide mass and the water, we apply a general two-phase mass flow model (Pudasaini in J Geophys Res 117:F03010, 2012. <https://doi.org/10.1029/2011JF002186>) and present high-resolution novel simulation results for a two-phase landslide impacting a fluid reservoir. Our simulations demonstrate that the intense flow-obstacle-interaction dramatically reduces the flow momentum resulting in the rapid energy dissipation around the obstacles. With the increase in obstacle height, overtopping decreases, but the deflection and capturing (holding) of solid mass

J. Kafle (✉) · P. Kattel
School of Science, Kathmandu University, Budol, Dhulikhel, Kavrepalanchok, Nepal
E-mail: jkafle@student.ku.edu.np

J. Kafle
Central Department of Mathematics, Tribhuvan University, Kirtipur, Kathmandu, Nepal

P. Kattel
Department of Mathematics, Tri-Chandra Multiple Campus, Tribhuvan University, Kathmandu, Nepal

M. Mergili
Institute of Applied Geology, University of Natural Resources and Life Sciences (BOKU), Vienna, Austria

M. Mergili
Geomorphological Systems and Risk Research (ENGAGE), Department of Geography and Regional Research,
University of Vienna, Universitätsstraße 7, 1010 Vienna, Austria

J.-T. Fischer
Department of Natural Hazards, Austrian Research Center for Forests - BFW, Rennweg 1, 6020 Innsbruck, Austria

S.P. Pudasaini
Institute of Geosciences and Meteorology, Geophysics Section, University of Bonn, Meckenheimer Allee 176, 53115 Bonn,
Germany

increases. Due to multiple obstacles, the moving mass decreases both in amount and speed showing fingering and meandering multiple streambed lobes. The varying location of the obstacles changes the deflection pattern, holding of mass, and tsunami intensity and mobility. Our simulations and findings enrich our understanding of mixing and separation between phases, generation and propagation of special solid and fluid structures, and transitions during the flow process, that may form a basis for the hazard mitigation in coastal regions.

1 Introduction

Tsunamis are triggered by impulsive geological events such as sea floor deformation due to earthquakes, landslides, volcanic eruptions, meteorite impacts, and underwater explosions [8, 43, 50, 78]. In the present work, we focus on landslide-triggered tsunamis in mountain lakes or reservoirs. The impact of the landslide into a water body results in an initial wave crest [50, 77]. Among the tsunamis caused by different geophysical events, landslide-generated tsunamis are much more localized and may cause more local threats than earthquake-generated tsunamis [21, 64, 70].

Various types of subaerial and submarine landslides can be described as gravitational mass flows. These potentially catastrophic processes show variable flow behavior and are generally unsteady, multi-phase, and rheologically complex [79]. They are often characterized by flows of a mixture of more or less viscous fluid and solid particles of various size down a slope [29, 56, 60, 61, 68]. The mechanically weaker viscous fluid and stronger solid particles evolve differently in terms of flow dynamics.

Mountain areas are often characterized by numerous large rivers and lakes, including glacial lakes and artificial reservoirs created for hydroelectric power generation [2, 3, 38, 48, 55, 73, 76]. The interaction of landslides with water bodies may result in tsunamis or, more specifically, impact waves [25, 26, 39, 61]. Depending on the initial position of the triggered landslide, the landslide–water interaction can be categorized as subaerial, partially submerged, and submarine landslides [14, 33, 50]. Subaerial and submarine landslides can create tsunamis as they transfer their impact energy to the water body [36, 43, 45, 46, 78]. This results in impact waves that cause devastation mainly due to run-up along the shoreline, overtopping of dams [2, 72], subsequent dam breaking [46], and flooding [78]. The significant energy carried by tsunami propagation can cause damages and casualties both nearby and far downstream, threatening human life as well as critical infrastructures [5, 16, 20, 26, 44, 50, 74].

Figure 1A, as an example, shows the Vajont Dam (Italy) before the disaster of October 9, 1963. Approximately $2.6 \times 10^8 \text{ m}^3$ of rock broke off from the slope of Monte Toc, and plunged into the reservoir. Even though the dam withstood the hydraulic pressure and suffered only minor damages (Fig. 1B), the landslide impact resulted in a massive wave of at least $5 \times 10^9 \text{ m}^3$ of water. The subsequent flood completely destroyed the village of Longarone in the Piave Valley and claimed approx. 2000 human lives [73, 75].

The landslide-tsunami generation and propagation process may involve various phenomena in chain: the landslide dynamics, energy transfer from landslide to water body, tsunami wave generation, submarine mass flow, potential obstacle-interactions, tsunami propagation and run-up along the shores [45, 46]. Landslide-impact-generated tsunamis and submarine mass flows are more complex than subaerial landslides. The situation is even more complex when the submarine flow and tsunami interacts with obstacles. But, these are technically

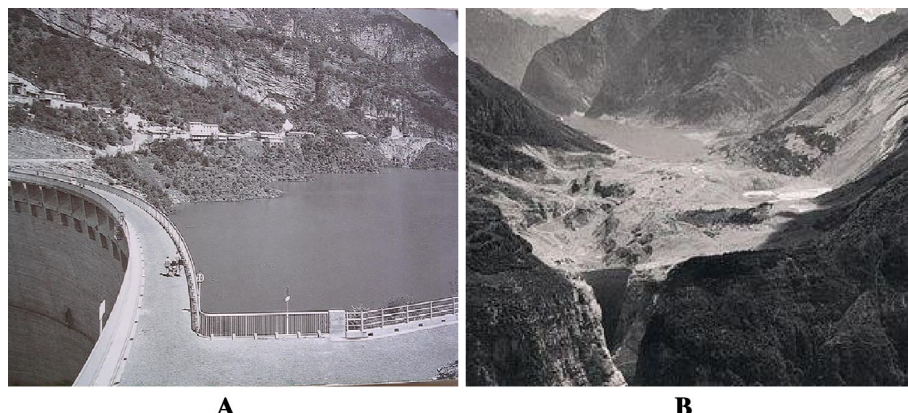


Fig. 1 Vajont dam and reservoir **A:** before the landslide, **B:** after the landslide (Von Hardenberg [73])

very important aspects. Boulders, fiber-optics, oil-drilling platforms, oil pipe lines, wind farms are some obstacles found in water bodies [13]. In a tsunami-prone water reservoir, obstacles may be constructed inside the water body or in bay-mouths as wave-breaking barriers as a mitigative measure to substantially alter the mass flow dynamics. At the same time, the obstacles may be damaged by the tsunami and submarine landslide impacts [13,67]. Installing obstacles in a water body is especially needed when the subaerial coastal slope stabilization and construction of obstacles in the subaerial slope are not feasible. The reduction of the wave velocity is the main way to minimize damages of the coastal infrastructures.

The study of debris flow past subaerial obstacles has drawn much more attention in recent years, because of its importance in the design of man-made structures like deflecting and catching dams and braking mounds [9,32,59]. It is even more dangerous if the flowing mass overtops the defense structures [2] and if the flow also generates shock waves [6]. The obstacle interaction with solid and fluid material may be fundamentally different as solid particles are frictional material and are probably obstructed more than the fluid by the obstacles. Also, the interaction of solid with obstacle can be more complex than the same with the fluid. Kattel et al. [35] presented first ever two-phase debris flow-obstacle-interaction for subaerial flow. However, there exists no research investigating real two-phase mass impacting a reservoir and interacting with submarine obstacles. So, there is a need for a reliable prediction of the complex dynamics of two-phase submarine mass flows and the subsequent submarine obstacle-interactions with robust numerical tools to predict and mitigate the hazard induced by the catastrophic events, and at the same time to optimize the strategy of defense measures [44,59].

In the past, numerical simulations were largely based on effectively single-phase shallow water and/or granular flow models to describe fluid and solid motions, submarine landslides, and tsunami. The utilized models include the incompressible Navier–Stokes equations [27], shallow water equations [28,31], smoothed particle hydrodynamics [51], the finite-volume method for three-dimensional slides [40], and a finite-volume method based on multiple-fluid Navier–Stokes equations [1]. Savage and Hutter developed a depth-averaged continuum mechanical model to describe the flow of granular materials [65,66]. This model was later extended geometrically to two and three dimensions [18,57,59,69]. The Coulomb mixture models of Iverson and Denlinger [30] and their extension by Pudasaini et al. [58] allow basal pore fluid pressure to evolve and include viscous effects. However, these are virtually single-phase debris bulk models, as they could not include the differences between the fluid- and solid-velocities. Pitman and Le [56] developed a two-fluid model that includes simple drag force to describe flows as a mixture of the solid particles and the fluid. But, they neglected the viscous fluid effects.

Jiang and LeBlond [31] proposed a two-layer model, where the lower-layer landslide was treated either as a laminar incompressible viscous or visco-plastic fluid, with which the deformable submarine landslide and associated tsunamis were dynamically coupled. Ma et al. [42] presented a shock-capturing three-dimensional non-hydrostatic, fully dispersive surface wave model. The governing equations are the incompressible Navier–Stokes equations written in surface and terrain-following form, with turbulent diffusion. The model has been applied to simulate landslide-generated tsunami [22,23,37,43] and is validated based on analytical solutions and experimental data. They presented more realistic landslide-generated waves using a non-hydrostatic model. However, in their approach there are no dynamic interactions between the landslide mass and the water except the prescribed landslide motion locally changes free surface height of the water leading to the tsunami waves. Furthermore, Ma et al. [43] presented a depth-averaged computational model for two-layer granular landslide for tsunami wave generation. They described the landslide as a saturated Coulomb frictional granular flow (effectively single-phase mixture) as represented by bulk mixture density, velocity, and stress [29,30,58], which, however, do not include particle fluid interactions. Tsunami wave generation is simulated by the Ma et al. [42] model. Dynamic interactions between the landslide and water are accounted for by imposing continuity of normal stress at the interface, and the kinematic interfacial constraints for each layer. The model is tested against an analytical solution for granular dam-break flow and laboratory experiments on impulsive wave generation by subaerial granular landslides, and they could reasonably well predict both the tsunami wave generation and the granular landslide dynamics. In the comparison, the final deposition was found to be located at the plane bed close to the transition of the slope, which is more offshore than that observed in the experiments [49], probably due to their model which neglected the additional friction due to the slope curvature [12]. This discrepancy might indicate for including additional effects such as the interfacial drag, ambient drag, and other interfacial momentum exchanges [60]. Where the existing approaches [22,23,37,42,43] have been shown to be useful for landslide mass that remains intact, their model cannot be applied when mixing between the landslide and the impacted water body is substantial, and when the landslide mass itself is more dilute. For example, a regularization term of leading order was artificially introduced [37] in order to control the diffusion

of the landslide volume. Grilli et al. [23] performed numerical simulations to assess coastal tsunami hazard by performing tsunami simulations with the Boussinesq long-wave model.

Yavari-Ramshe and Ataei-Ashtiani [78] presented a very detailed review of numerical modeling of subaerial and submarine landslide-generated tsunamis focusing on recent advances and future challenges. The review scrutinized the main landslide events followed by landslide-generated wave hazard. Interestingly, with the majority of data, they justified the application of the most often used depth-averaged equations and simulations for landslide motion.

However, many existing models, including Ma et al. [43], ignored the stresses and mixing at the landslide–water interface. These effects are included in our model formulation [60] and the resulting simulations. Existing approaches cannot take into account other important aspects of interfacial momentum transfer in mixture flows, such as interfacial drag, buoyancy, mobility of the fluid at the particle surface, and virtual mass force, that play important roles in the correct prediction of mixture flow dynamics [33,34,45,47,60,62]. Although we do not explicitly distinguish between the submerged landslide and upper water layer, we can deal with different mixtures in the landslide and fluid body, from dry to dense to dilute mixtures with strong interfacial momentum transfer between the solid (particle) and viscous fluid phases. Furthermore, our model includes both the Newtonian and non-Newtonian viscous stresses.

Pudasaini [60] developed a generalized two-phase mass flow model unifying existing avalanche and debris flow theories, which includes buoyancy, and three other dominant physical aspects of non-Newtonian viscous stress, virtual mass, and generalized drag. These make the model suitable to study a wide range of geophysical mass flows. During the motion of two-phase landslide and debris flow, one phase (e.g., solid) may accelerate relative to the other phase (e.g., fluid). This induces virtual mass. The quantity and concentration gradient of the solid particles affects the flow substantially and can increase or reduce viscous effects. A generalized interfacial momentum transfer should include viscous drag, buoyancy, and virtual mass forces, and a generalized drag force should combine the solid- and fluid-like contributions according to the constituent composition and flow situation. All these aspects have been incorporated only in the two-phase mass flow model by Pudasaini [60]. The advantage of the two-phase debris flow model over classical single-phase or quasi-two-phase models is that the composition of initial debris mass can be described by using the solid volume fraction. The different values of the solid volume fraction can describe a dry (landslide or rock slide), a fluid or hyper-concentrated flow (water or muddy water, e.g., reservoirs and rivers), and a general debris mixture of different solid concentrations as needed in real flow situations. Most of the existing researches related to landslide-generated tsunami have coupled the landslide and still water with resulting tsunamis modeled differently [22,23,31,42,43,50], but our formulation [45,46,61] makes simultaneous simulations (within a single framework) of the sliding debris (or, landslide), the lake or ocean, the debris impact at the lake or ocean, the tsunami generation and propagation, the mixing and separation between the solid and fluid phases, and the sediment transport and halting processes in the bathymetric surface.

Utilizing the Pudasaini [60] model, a geometrically two-dimensional, two-phase subaerial debris flow impacting a two-dimensional reservoir, tsunami generation and propagation, and submarine mass flow has been presented in Pudasaini [61]. Further advancement is made by focusing on geometrically three-dimensional aspects of such complex flows and the related impulsive water waves. The detailed analysis of how the positions of initial debris mass on the inclined slope influence the splash, tsunami generation, and debris mass movements in reservoir were done by Kafle et al. [33]. The model has also been applied to flow-obstacle-interactions in Kattel et al. [35] where a set of numerical experiments was carried out to analyze mass deflection, and redirection and phase separation of two-phase debris mass interacting with tetrahedral structures in subaerial slope. The ratios of the obstacle heights to the incoming flow depths as functions of incoming flow Froude number are in line with the phase diagram in Faug [11], constructed from the depth-averaged analytic solution for dry granular flows.

To justify the functionalities of the GIS-based open source computational tool r.avaflood, that employs the enhanced version of two-phase mass flow model of Pudasaini [60], Mergili et al. [45] performed two sets of computational experiments—the first as a generic process chains consisting in bulk mass and hydrograph release into a reservoir with entrainment of the dam and impact downstream, and the second as the back analysis of the prehistoric Acheron rock avalanche of New Zealand. In the first case, they obtained plausible simulation results. Also, by the optimization of key parameters, the produced simulations were in line with the corresponding observations for the second case. Employing the same model and the computational tool, Mergili et al. [46] back-calculated a geological event, where a landslide from a moraine slope triggered a multi-lake outburst flood in the Artizón and Santa Cruz valleys, Cordillera Blanca, Peru (2012). The reconstructed flow patterns were largely found in line with the documented geomorphologic changes induced by the event.

Mergili et al. [47] simulated complex flow-dominated landslides by back-calculating the Huascarán (Cordillera Blanca, Peru) events of 1962 and 1970 with r.avaflow, and the two-phase mass flow model [60] with optimized parameter set mainly for basal friction and entrainment coefficient. The results reproduced the spatial and temporal evolution of flow depths, flow velocities, travel times, and volumes of the events reasonably well and also highlighted some challenges and uncertainties in simulating the complex mass flow events.

To analyze the run-out characteristics of the catastrophic landslide that occurred in 2015 at Hongao construction waste dumpsite in the Guangming New District of Shenzhen, China, Qiao et al. [63] also used the computational tool, r.avaflow utilizing the two-phase mass flows model [60] and simulated the case with the variation of solid density, solid volume fraction, and the complex drag. They mainly focused on the evolution of the flow depth, velocity, and pressure. Their simulations showed that the variation of solid density influenced much more in the deposition area. Larger solid density resulted in the reduced travel distance and narrower spreading range as the effect of buoyancy in the landslide motion. Decreasing drag intensity enhanced the fluid pressure and velocity. Furthermore, Bout et al. [4] integrated the two-phase debris flow model [60] in a catchment model for flashfloods, debris flows, and shallow slope failures. With this, they developed an integrated modeling method for shallow landslides, debris flows, and catchment hydrology. The method coupled the two-phase debris flow equations [60] and an infinite slope method with a full hydrological catchment model. The novel approach was tested with the 4 km² Scaletta catchment, Sicily-Italy, where the 2009 storm caused hundreds of shallow landslides and debris flooding. Validation shows that the model can recreate the impact of both shallow landslides, debris flow run-out, and debris floods by well reproducing the general patterns of slope failure and run-out. This led to a fully physically based prediction method of rainfall induced debris flood behavior in the downstream areas, including the formation of debris fan at the coastal outlet. These are the reasons for choosing the two-phase mass flow model of Pudasaini [60] to simulate submarine mass movement and tsunami impact on submarine obstacles.

A more accurate description can only be achieved with full-dimensional simulation. Similarly, frequency dispersion is an important aspect in landslide-generated tsunami [17, 21, 23, 37, 41–43]. These aspects, however, are not within the scope here, and will be dealt with separately using real two-phase mass flows, which is still in the early stage of development as mostly such simulations have been performed with single-phase models.

We present high-resolution, novel simulation results for a real two-phase debris mass impacting a fluid reservoir containing obstacles of different sizes, dimensions and numbers, installed at different positions both in subaerial slopes and in bathymetric surface. The effects of the obstacles in the water body and on the slope surface, and the resulting intensity of tsunami and its propagation will be analyzed in detail. The objective of this work is to assess the potential of the two-phase model [60] to study the effects of obstacles in submarine mass movement and the tsunami propagation. This will provide us with the first ever basic features of flow-obstacle-interaction in submarine environment.

2 Physical–mathematical model

2.1 Model equations

In the following, we briefly mention the general two-phase mass flow model developed by Pudasaini [60]. In a two-phase debris mixture, the two phases particle–viscous fluid are described by different material properties. The fluid phase is characterized by its material density ρ_f , viscosity η_f , and isotropic stress distribution. The solid phase is characterized by its material density ρ_s , internal friction angle ϕ , the basal friction angle δ , and an anisotropic stress distribution through the lateral earth pressure coefficient K . In Eqs. (1)–(6), x , y , and z are coordinates along the down-slope, cross-slope, and the surface normal direction, respectively; g^x , g^y , and g^z are the respective components of gravitational acceleration, and the subscripts s and f stand for the solid and the fluid phases, and $\mathbf{u}_f = (u_f, v_f)$ and $\mathbf{u}_s = (u_s, v_s)$ are the depth-averaged velocity components for fluid and for solid in the down-slope (x) and the cross-slope (y) directions, respectively. The flow depth is h , α_s is the solid volume fraction, and $\alpha_f = 1 - \alpha_s$ is the fluid volume fraction. The nonlinear partial differential equations representing mass and momentum balances for solid and fluid in the down-slope and the cross-slope directions are given by [60]

$$\frac{\partial}{\partial t}(\alpha_s h) + \frac{\partial}{\partial x}(\alpha_s h u_s) + \frac{\partial}{\partial y}(\alpha_s h v_s) = 0, \quad (1)$$

$$\frac{\partial}{\partial t}(\alpha_f h) + \frac{\partial}{\partial x}(\alpha_f h u_f) + \frac{\partial}{\partial y}(\alpha_f h v_f) = 0, \quad (2)$$

$$\begin{aligned} \frac{\partial}{\partial t} [\alpha_s h (u_s - \gamma \mathcal{C}(u_f - u_s))] + \frac{\partial}{\partial x} \left[\alpha_s h \left(u_s^2 - \gamma \mathcal{C}(u_f^2 - u_s^2) + \frac{1}{2} \beta_{x_s} h \right) \right] \\ + \frac{\partial}{\partial y} [\alpha_s h (u_s v_s - \gamma \mathcal{C}(u_f v_f - u_s v_s))] = h S_{x_s}, \end{aligned} \quad (3)$$

$$\begin{aligned} \frac{\partial}{\partial t} [\alpha_s h (v_s - \gamma \mathcal{C}(v_f - v_s))] + \frac{\partial}{\partial x} \left[\alpha_s h (u_s v_s - \gamma \mathcal{C}(u_f v_f - u_s v_s)) \right] \\ + \frac{\partial}{\partial y} \left[\alpha_s h \left(v_s^2 - \gamma \mathcal{C}(v_f^2 - v_s^2) + \frac{1}{2} \beta_{y_s} h \right) \right] = h S_{y_s}, \end{aligned} \quad (4)$$

$$\begin{aligned} \frac{\partial}{\partial t} \left[\alpha_f h \left(u_f + \frac{\alpha_s}{\alpha_f} \mathcal{C}(u_f - u_s) \right) \right] + \frac{\partial}{\partial x} \left[\alpha_f h \left(u_f^2 + \frac{\alpha_s}{\alpha_f} \mathcal{C}(u_f^2 - u_s^2) + \frac{1}{2} \beta_{x_f} h \right) \right] \\ + \frac{\partial}{\partial y} \left[\alpha_f h \left(u_f v_f + \frac{\alpha_s}{\alpha_f} \mathcal{C}(u_f v_f - u_s v_s) \right) \right] = h S_{x_f}, \end{aligned} \quad (5)$$

$$\begin{aligned} \frac{\partial}{\partial t} \left[\alpha_f h \left(v_f + \frac{\alpha_s}{\alpha_f} \mathcal{C}(v_f - v_s) \right) \right] + \frac{\partial}{\partial x} \left[\alpha_f h \left(u_f v_f + \frac{\alpha_s}{\alpha_f} \mathcal{C}(u_f v_f - u_s v_s) \right) \right] \\ + \frac{\partial}{\partial y} \left[\alpha_f h \left(v_f^2 + \frac{\alpha_s}{\alpha_f} \mathcal{C}(v_f^2 - v_s^2) + \frac{1}{2} \beta_{y_f} h \right) \right] = h S_{y_f}, \end{aligned} \quad (6)$$

in which

$$\beta_{x_s} = \varepsilon K_x p_{b_s}, \quad \beta_{y_s} = \varepsilon K_y p_{b_s}, \quad \beta_{x_f} = \beta_{y_f} = \varepsilon p_{b_f}, \quad p_{b_f} = -g^z, \quad p_{b_s} = (1 - \gamma) p_{b_f}.$$

Here, p_{b_f} and p_{b_s} are the effective fluid and solid pressures at the base. Equations (1)–(2) are depth-averaged mass balance equations for solid and fluid phases, respectively. The last four equations are depth-averaged momentum balances for solid (3)–(4) and fluid (5)–(6) in the x - and y -direction, respectively. The source terms are [60]:

$$S_{x_s} = \alpha_s \left[g^x - p_{b_s} \left(\frac{u_s}{|\mathbf{u}_s|} \tan \delta + \varepsilon \frac{\partial b}{\partial x} \right) \right] - \varepsilon \alpha_s \gamma p_{b_f} \left[\frac{\partial h}{\partial x} + \frac{\partial b}{\partial x} \right] + C_{DG}(u_f - u_s) |\mathbf{u}_f - \mathbf{u}_s|^{J-1}, \quad (7)$$

$$S_{y_s} = \alpha_s \left[g^y - p_{b_s} \left(\frac{v_s}{|\mathbf{u}_s|} \tan \delta + \varepsilon \frac{\partial b}{\partial y} \right) \right] - \varepsilon \alpha_s \gamma p_{b_f} \left[\frac{\partial h}{\partial y} + \frac{\partial b}{\partial y} \right] + C_{DG}(v_f - v_s) |\mathbf{u}_f - \mathbf{u}_s|^{J-1}, \quad (8)$$

$$\begin{aligned} S_{x_f} = \alpha_f \left[g^x - \varepsilon \left[\frac{1}{2} p_{b_f} \frac{h}{\alpha_f} \frac{\partial \alpha_s}{\partial x} + p_{b_f} \frac{\partial b}{\partial x} - \frac{1}{\alpha_f N_R} \left\{ 2 \frac{\partial^2 u_f}{\partial x^2} + \frac{\partial^2 v_f}{\partial y \partial x} + \frac{\partial^2 u_f}{\partial y^2} - \frac{\chi u_f}{\varepsilon^2 h^2} \right\} \right. \right. \\ \left. \left. + \frac{1}{\alpha_f N_{R_A}} \left\{ 2 \frac{\partial}{\partial x} \left(\frac{\partial \alpha_s}{\partial x} (u_f - u_s) \right) + \frac{\partial}{\partial y} \left(\frac{\partial \alpha_s}{\partial x} (v_f - v_s) + \frac{\partial \alpha_s}{\partial y} (u_f - u_s) \right) \right\} \right. \right. \\ \left. \left. - \frac{\xi \alpha_s (u_f - u_s)}{\varepsilon^2 \alpha_f N_{R_A} h^2} \right] \right] - \frac{1}{\gamma} C_{DG}(u_f - u_s) |\mathbf{u}_f - \mathbf{u}_s|^{J-1}, \end{aligned} \quad (9)$$

$$\begin{aligned} S_{y_f} = \alpha_f \left[g^y - \varepsilon \left[\frac{1}{2} p_{b_f} \frac{h}{\alpha_f} \frac{\partial \alpha_s}{\partial y} + p_{b_f} \frac{\partial b}{\partial y} - \frac{1}{\alpha_f N_R} \left\{ 2 \frac{\partial^2 v_f}{\partial y^2} + \frac{\partial^2 u_f}{\partial x \partial y} + \frac{\partial^2 v_f}{\partial x^2} - \frac{\chi v_f}{\varepsilon^2 h^2} \right\} \right. \right. \\ \left. \left. + \frac{1}{\alpha_f N_{R_A}} \left\{ 2 \frac{\partial}{\partial y} \left(\frac{\partial \alpha_s}{\partial y} (v_f - v_s) \right) + \frac{\partial}{\partial x} \left(\frac{\partial \alpha_s}{\partial y} (u_f - u_s) + \frac{\partial \alpha_s}{\partial x} (v_f - v_s) \right) \right\} \right. \right. \\ \left. \left. - \frac{\xi \alpha_s (v_f - v_s)}{\varepsilon^2 \alpha_f N_{R_A} h^2} \right] \right] - \frac{1}{\gamma} C_{DG}(v_f - v_s) |\mathbf{u}_f - \mathbf{u}_s|^{J-1} \end{aligned} \quad (10)$$

where

$$\begin{aligned} C_{DG} &= \frac{\alpha_s \alpha_f (1 - \gamma)}{[\varepsilon \mathcal{U}_T \{\mathcal{P} \mathcal{F}(Re_p) + (1 - \mathcal{P}) \mathcal{G}(Re_p)\}]^J}, \quad \gamma = \frac{\rho_f}{\rho_s}, \quad \mathcal{F} = \frac{\gamma}{180} \left(\frac{\alpha_f}{\alpha_s} \right)^3 Re_p, \\ \mathcal{G} &= \alpha_f^{M(Re_p)-1}, \quad Re_p = \frac{\rho_f d \mathcal{U}_T}{\eta_f}, \quad N_R = \frac{\sqrt{gLH} \rho_f}{\alpha_f \eta_f}, \quad N_{RA} = \frac{\sqrt{gLH} \rho_f}{A \eta_f}. \end{aligned} \quad (11)$$

L and H are the typical length and depth of the flow, $\varepsilon = H/L$ is the aspect ratio, and $\mu = \tan \delta$ is the basal friction coefficient. The generalized drag coefficient C_{DG} is modeled by a linear combination with $\mathcal{P} \in [0, 1]$ of the solid-like (\mathcal{G}) and fluid-like (\mathcal{F}) drag contributions to flow resistance. $J = 1$ or 2 represents simple linear or quadratic drag. \mathcal{U}_T is the terminal velocity of a particle. γ is the density ratio, \mathcal{C} is the virtual mass coefficient (enhanced kinetic energy of the fluid phase induced by solid particles), M is a function of the particle Reynolds number (Re_p), χ includes vertical shearing of fluid velocity, and ξ takes into account different distributions of α_s . A is the mobility of the fluid at the interface, and N_R and N_{RA} are, respectively, the quasi-Reynolds number and mobility-Reynolds number associated with the classical Newtonian and enhanced non-Newtonian fluid viscous stresses. Slope topography is given by $b = b(x, y)$.

2.2 Obstacle

Geophysical mass flows may encounter different types of obstacles [10, 19, 59]. In our simulations (Section 3.3), we use differently sized circular bumps of different radii and heights as obstacles. The main reason for choosing the circular bumps as subaerial and submarine obstacle is that the boulders can be approximated by three-dimensional circular bumps [53, 71]. We use the bump as

$$b(x, y) = H \times \exp \left(-\frac{1}{[r^2 - \{(x - x_0)^2 + (y - y_0)^2\}]} \right), \quad (12)$$

with the center at $(x_0, y_0, 0)$, radius r , and height $H_c = H \times \exp(-1/r^2)$ at the bump center (see, Fig. 2B). The bump locally changes the topographic gradient of the slope. The bump-induced spatial derivatives $\partial b / \partial x$ and $\partial b / \partial y$ enter the model Eqs. (7)–(10) to account for two-phase flow-obstacle-interactions.

3 Simulating two-phase debris flow and submarine obstacle interactions

Here, we present geometrically three-dimensional, high-resolution simulation results for a two-phase debris mass impacting a fluid reservoir. Obstacles of different shapes, sizes, and numbers are installed at different subaerial and bathymetric positions. We also analyze the tsunami and submarine flow dynamics around the obstacle, and in the flow influence region, tsunami wave impact, and the depositional behavior of the debris material in the reservoir with obstacles as compared to the reservoirs without obstacles.

3.1 Numerical method

The model Eqs. (1)–(6) are written as well-structured, nonlinear hyperbolic–parabolic partial differential equations in conservative form [60]. The model is used to compute the debris depth h , solid volume fraction α_s , velocity components for solid (u_s, v_s), and for fluid (u_f, v_f) in x - and y -direction, respectively, as functions of space and time (Fig. 2A). The model equations are solved in conservative variables $\mathbf{W} = (h_s, h_f, m_{s_x}, m_{f_x}, m_{s_y}, m_{f_y})^t$, where $h_s = \alpha_s h$, $h_f = \alpha_f h$ are the solid and fluid contributions to the debris, or the flow height; and $m_{s_x} = \alpha_s h u_s$, $m_{f_x} = \alpha_f h u_f$; $m_{s_y} = \alpha_s h v_s$, $m_{f_y} = \alpha_f h v_f$ are, respectively, the solid and fluid momenta in x - and y -direction. This facilitates numerical integration even when shocks are formed in the field variables [60]. The high-resolution shock-capturing Total Variation Diminishing Non-Oscillatory Central (TVD-NOC) scheme [7, 59, 69] has been employed. Advantages of the applied unified simulation techniques and the corresponding computational strategy for real two-phase debris flows have been explained in Pudasaini [61]. This technique has been extended in Kattel et al. [34], Kafle et al. [33], and Mergili et

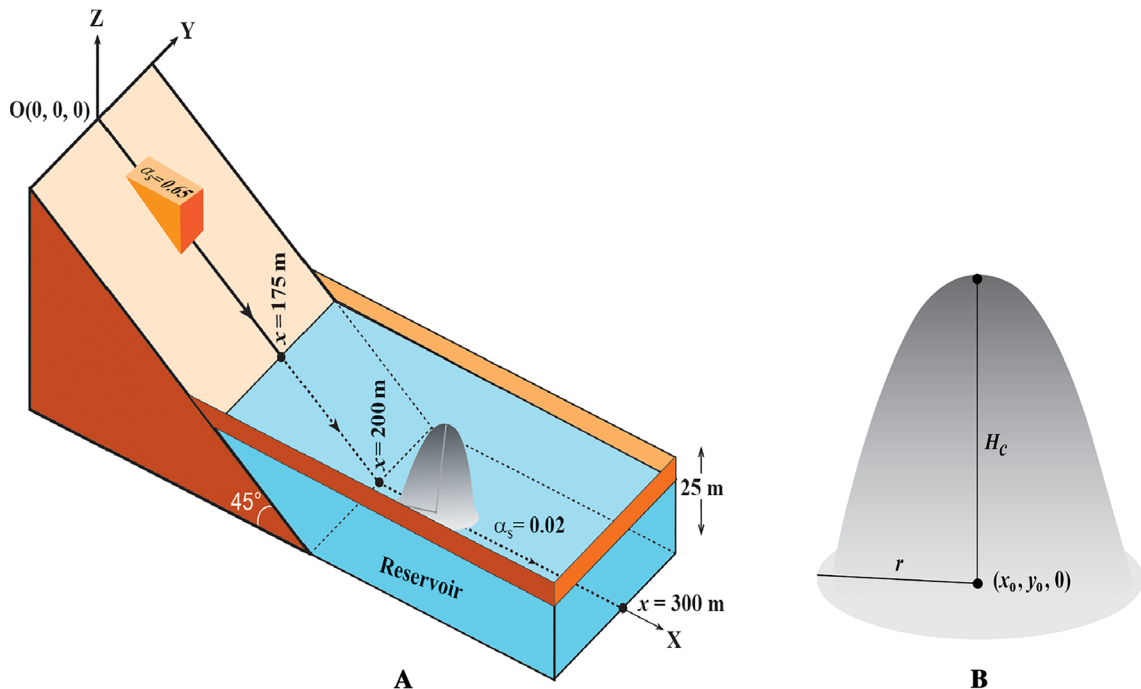


Fig. 2 **A** A sketch of the initial configuration of a debris mass on an inclined slab, a fluid reservoir in the downstream, and a circular bump as a submarine obstacle. Initially, the left end of the reservoir has the water height zero, which, due to the slope, gradually increases to its maximum height of 25 m from the down-slope coordinate $x = 175$ m to $x = 200$ m. Beyond this, from $x = 200$ m to $x = 300$ m, the initial fluid is at a constant height of 25 m. **B** A circular bump centered at $(x_0, y_0, 0)$, radius r and height H_c

al. [45, 46] for basic geometrically three-dimensional subaerial flows, submarine debris flows and subsequent tsunamis, and the interaction and propagation of mass flow in real mountain topographies and the complex hydro-geomorphic process chains.

3.2 Simulation setup and parameters

For all of our simulations, we consider a (geometrically) three-dimensional and two-phase subaerial debris flow that hits a fluid reservoir. The upper part of the channel is inclined downward ($\zeta_0 = 45^\circ$) to the right and is flat in the lateral direction (Fig. 2A). Initially at $t = 0$ s, the debris is in the form of a laterally spanned triangular wedge ($80 \text{ m} \leq x \leq 130 \text{ m}; -25 \text{ m} \leq y \leq 25 \text{ m}$). The initial debris mass in the upper part of the slope is uniformly distributed as a homogeneous mixture of 65% solid and 35% fluid. Similarly, initially the quiescent reservoir ($175 \text{ m} \leq x \leq 300 \text{ m}; -110 \text{ m} \leq y \leq 110 \text{ m}$) consists of 2% solid and 98% fluid. We consider such reservoir of finite length and width to model many natural and artificial reservoirs in the field scale [73, 75]. Moreover, the confined lateral boundaries are very much relevant to the mountain flanks of some real-world situations as in Fig. 1.

Thus, initially, the solid material height is given by

$$h_s = \begin{cases} 0.65(x - 80), & \text{for } 80 \leq x \leq 130; -25 \leq y \leq 25, \\ 0.02(x - 175), & \text{for } 175 \leq x \leq 200, \\ 0.02 \times 25, & \text{for } 200 \leq x \leq 300, \\ 0, & \text{elsewhere.} \end{cases} \quad (13)$$

Similarly, the fluid material height is given by

$$h_f = \begin{cases} 0.35(x - 80), & \text{for } 80 \leq x \leq 130; -25 \leq y \leq 25, \\ 0.98(x - 175), & \text{for } 175 \leq x \leq 200, \\ 0.98 \times 25, & \text{for } 200 \leq x \leq 300, \\ 0, & \text{elsewhere.} \end{cases} \quad (14)$$

The other parameter values chosen for simulation are $\phi = 45^\circ$, $\delta = 15^\circ$, $\rho_f = 1100 \text{ kgm}^{-3}$, $\rho_s = 2900 \text{ kgm}^{-3}$, $N_R = 30,000$, $N_{RA} = 1000$, $Re_p = 1$, $U_T = 5.0 \text{ ms}^{-1}$, $\mathcal{P} = 0.75$, $J = 1$, $\chi = 3$, $\xi = 5$, $\mathcal{C} = 0.5$. Note that, for simplicity, here we consider the linear drag. These parameter selections are based on the physics of the two-phase subaerial and submarine mass flows [33,34,45,60–62].

3.3 Simulation results and discussion

Terminology, scope, and limitation of the approach: Before presenting the simulation results, to avoid any possible ambiguity, we explain the use of some terminology that might differ from those in usual consideration in submarine landslides. We try to make the description as reasonable and representative as possible within the context of this contribution. As the debris mixture impacts the water body, locally, at any position, the change in the solid concentration is smaller as compared to reservoir fluid level that is substantially larger. But, as the debris mixture penetrates the reservoir, the water column above it is automatically increased to enhance the local fluid depth h_f . So, due to the enhanced solid and fluid heights, or the total debris $h = h_s + h_f$, the surface water wave (tsunami) is generated in terms of surface wave or a concentration shock, respectively. The term submarine mass flow is used to recognize the amount of the solid volume fraction in the water body but, not as the bottom layer of solid material (dense landslide), overlaid by the water layer as in two-layer models [22,23,37,42,43]. Similarly, the term deposition is associated with the stopping process of the solid (or fluid) as the local velocity becomes zero (or negligible, i.e., below a numerical threshold). Solid particles halt due to friction, but fluid moves until pressure gradients vanish, or until they are balanced by gravitational forces. However, deposition here is not associated with the settling of the solid particles in the fluid as often used in full-dimensional simulations in particle–fluid mixture flows [33,34,45,47,60,62]. Such settling has not been included in the present depth-averaged simulations. These terms are used only for convenience of the interpretation of the results. Importantly, we mention that, at a given position of the basal surface, we can only obtain the solid and fluid content in the total debris mixture, but they are not separated to form a two-layer flow as soon as the subaerial debris flow plunges into the water body. However, such reorganization is convenient for the visualization. Similarly, no vertical velocity stratifications are resolved (or captured) by the present depth-averaged simulation approach which requires the full three-dimensional simulations [42,43]. This is not within the scope here.

The general structure of the depth-averaged model equations is that we do not have the possibility for the explicit formation of the layered solid and fluid materials, and thus, no description of the interface between the solid and fluid layers can be provided. Furthermore, except the parameterizations, we do not have the description of distribution of the solid fraction in the flow depth direction; only information on the amount of solid and fluid component is available at a given position along the (bathymetric) slope. However, for the visualization, it is convenient to separately plot the solid and fluid phases as done here, but with the recognition that they only represent the local amounts of solid and fluid, and they are not separated, rather mixed with unknown solid concentration distributions in the flow depth direction.

We interpret that the penetrating debris mixture interacts with the entire height of the obstacle if the obstacle height is less than or equal to the height of the impacting debris. But, if the obstacle height is larger than the fluid height h_f , or the surface tsunami, then only that height of the obstacle is impacted by the mixture flow. In both situations, the motions of the effective solid and fluid components or heights in the mixture are influenced by the obstacles by the dissipative terms $\partial b/\partial x$ and $\partial b/\partial y$.

First, we present a reference simulation when the reservoir contains no obstacle. Then, we mainly study the effects of obstacles in the tsunami generation, amplification, and propagation, and the submarine debris-obstacle-interaction. Furthermore, we analyze how the number, size, and location of obstacles influence the submarine debris (landslide) dynamics and depositional behavior.

3.3.1 Reservoir without obstacle

Figure 3 presents some basic results in terms of the total debris depth (the sum of the solid and the fluid depths) along with the evolution of the solid phase, the penetration of the debris into the reservoir without obstacles, the debris flow motion in the reservoir, and the complex wave interactions. From $t > 0$ s (left panel a), the debris mass has just started to deform and move down the inclined plane. As the mass is continuously spreading, the subaerial debris height has substantially decreased.

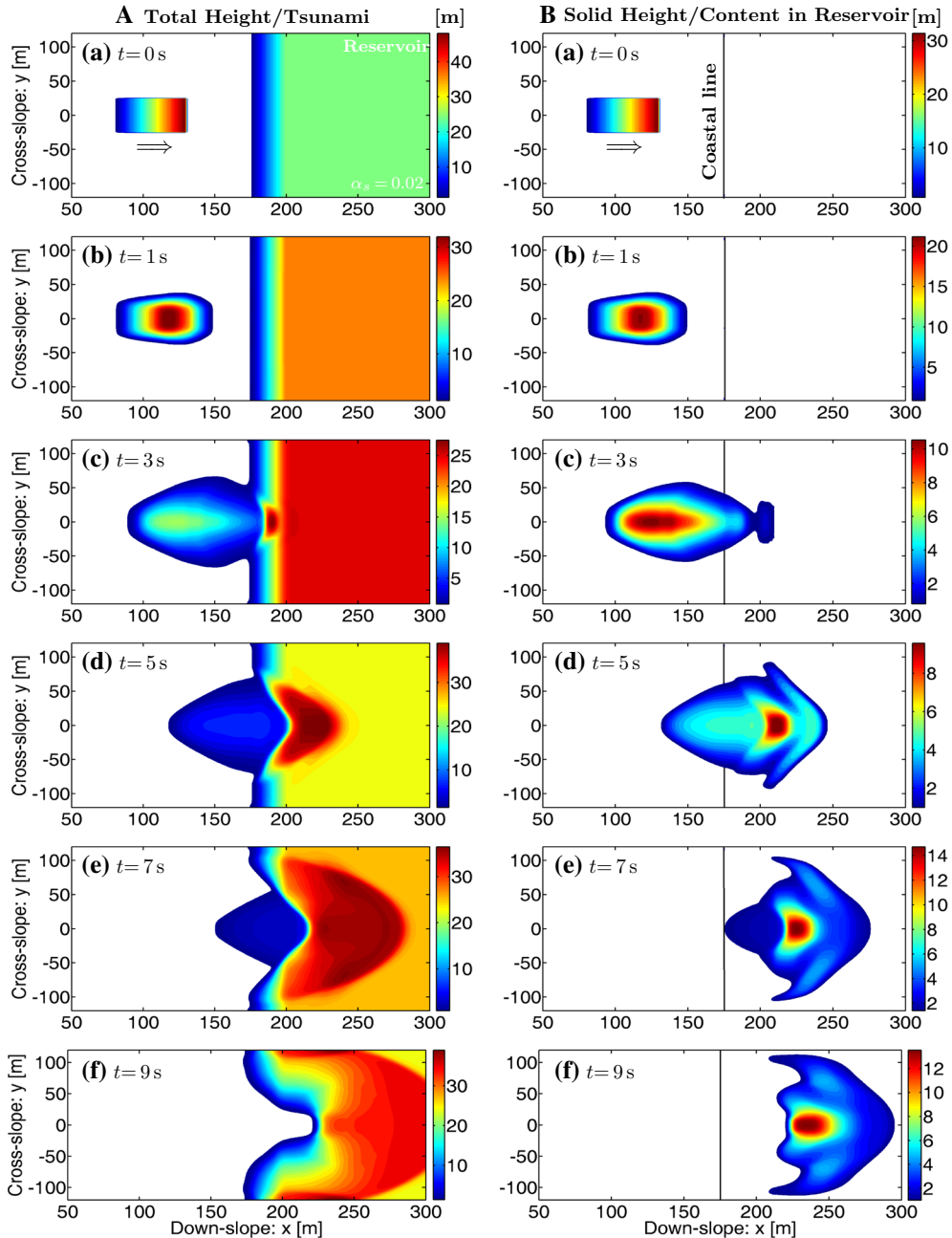


Fig. 3 **A** Total height of the debris mass and tsunamis when the reservoir is without obstacle. As time elapses, the formation, amplification, propagation, reflection, and intersection of coupled three-dimensional tsunamis are observed as subaerial two-phase debris mass impacts the quiescent water reservoir. **B** Evolution of the solid phase in the debris mixture in the reservoir. As soon as mass is released, the front is rarefied and accelerates. After $t > 3$ s, the solid mass forms a very special forward propagating laterally wide and curved wave of solid component (solid-wave). The arrows in the top panels indicate the flow direction

At $t = 1$ s, the debris height increases quickly from the front to the main body, whose maximum height appears to be closer to the frontal part of the debris than to the middle part. The debris height decreases as it advects down-slope and disperses cross-slope; the debris has already hit the center of the left coast of the reservoir to generate a tsunami at about $t = 3$ s. As the debris hits and penetrates the reservoir, the impacting mass generates tsunami that propagates immediately. Since the debris mass continuously hits the reservoir with higher momentum ($t = 5$ s, left panel d), the tsunami is expanded in the vicinity of the impact ($t = 7$ s, left panel e) and more and more fluid mass from the left of the reservoir is strongly pushed forward and laterally

during the flow. This produces a strong hydrodynamic impact vacuum [61] or crater [15], which increases and retains for some more time. For $3 \leq t \leq 9$ s, amplified three-dimensional tsunamis are clearly observed and three complex phenomena can be seen simultaneously: (i) a subaerial debris flow in the upstream region, (ii) submarine debris flow in the downstream region and in the reservoir, and (iii) a super-tsunami on the surface of the reservoir (the surface tsunami is on the order of 10–15 m). At $t = 5$ s, the height of the water surface has substantially increased due to the tsunami and the pushing of the water to the right (up to a bit more than $x = 240$ m) resulting in a maximum fluid height of about 38 m around $x = 240$ m. The color map shows that the tsunami propagates in all directions. The debris mass totally enters into the reservoir nearly at $t = 8$ s (not shown in Figure). The effect still persists in $t = 9$ s, showing impact vacuum. Due to downstream and lateral confinements in the reservoir, high-intensity tsunamis are observed near the lateral boundaries as shown by the color bar given alongside.

The fluid-only and the total geometric evolutions are qualitatively similar, so are not presented here. This is so because, with respect to the amount of the fluid in the reservoir, the fluid component (volume fraction) dominates the solid, and thus, the total and the fluid phase evolutions are very much similar [33]. However, the dynamics of the solid phase is completely different, mainly in the reservoir. The flow behavior of the solid-only part is presented in Fig. 3B as extracted from the total debris from Fig. 3A. As the mass is released, the front is rarefied and accelerating mainly due to the pressure gradient, and also due to the gravity, whereas the rear part takes some more time to spread and to slide down-slope due to the support of the mass from the front and the material frictions. After the mass is released, the front is propagating down-slope. However, from $t = 1$ s (right panel b) to $t = 3$ s (right panel c), the position of the relative maximum height has shifted a bit upslope. At $t = 5$ s (right panel d), the maximum height position is shifted down-slope as the initial solid mass in the rear part has moved down-slope. In Fig. 3B, maximum solid height has continuously decreased from 30 m at $t = 0$ s to 9 m at $t = 5$ s by its spreading, and increased to a bit more than 14 m at $t = 7$ s. But after $t = 5$ s (right panel d), it increases because the solid halting process has already begun. The near halted solid mass further disperses (spreads) in the down-slope and cross-slope direction, resulting in the decrease in solid height to nearly 13 m (at $t = 9$ s).

After $t = 3$ s, due to the impact of the subaerial debris on the reservoir, the solid mass has also been sheared and elongated cross-wise from the front to the middle portion ($t = 5$ s, right panel d), where the impact has influenced the dynamics. The lateral boundaries have also contributed to the lateral shearing. Due to the impact, the lateral spreading of the solid mass has increased from $t = 5$ s (right panel d) to $t = 9$ s (right panel f). At $t = 7$ s, the solid debris part has just crossed the coastal line ($x = 175$ m, the beginning of the reservoir water surface). This means, the solid component enters completely into the reservoir after $t = 7$ s (right panel e).

We also observe that the sliding mass changes its geometrical shape by its deformation mainly after it hits the fluid reservoir at $t = 3$ s. Due to the impact of the solid mass on the fluid reservoir, from $t = 5$ s to $t = 9$ s (right panel), it forms a very special forward propagating laterally wide and curved solid-wave. Figure 3B also shows the propagation of a turbidity current (low concentration of solid) and diffusion of the solid concentration waves in the front and the lateral margins. Also, strong and concentrated shock waves are developed in the vicinity of $x = 200$ m to $x = 250$ m after the debris mass reaches the horizontal portion of the reservoir.

3.3.2 A circular bump as an obstacle

In the simulation results presented in this Section, we consider a single three-dimensional circular bump of a fixed radius as an obstacle. But, we consider the bump of different heights at the same location and also the bump of the same height in different locations.

I. Reservoir containing a bump with different heights

Here, we analyze in detail the effects of the presence of bump with different heights as submarine obstacles in the reservoir. For comparison, we have kept the radius of the base constant (15 m).

A. Bump of height 15 m: First, we consider the case when the reservoir contains a totally submerged bump of height 15 m (Fig. 4). The center of the circular base is at (220, 0, 0) m. Panel (a) of Fig. 4A shows that initially the height of the mixture above the obstacle is 10 m with a total of 25 m (the reservoir height). In Fig. 4A, we observe that (after $t = 3$ s) the maximum of total flow height rapidly increases to 45 m at $t = 5$ s (left panel d) and then continuously decreases to 40 m and 39 m at $t = 7$ s and $t = 9$ s, respectively. This shows that the tsunami is more intensified in this case than in the previous case (Fig. 3). The deflection of the tsunami

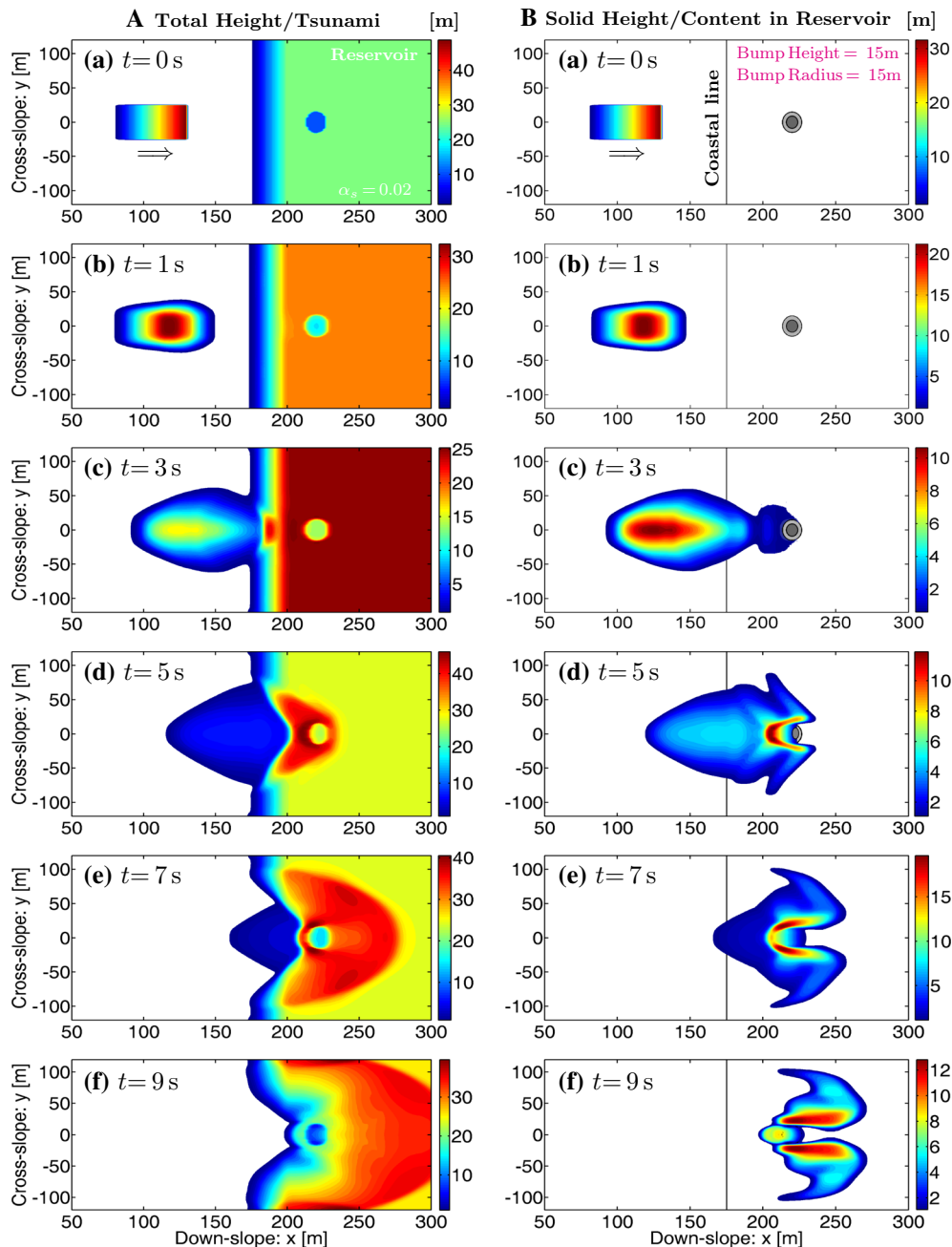


Fig. 4 **A** Total height of the debris mass and tsunamis when initially the reservoir contains a bump of height 15 m as a submarine obstacle with center at $(220, 0, 0)$ m. In this case, tsunami is less mobile than the previous case. **B** Evolution of the solid phase in the debris mixture in the reservoir. Due to presence of the obstacle, the major solid part of the debris mass is deflected into two lobes, and only a small solid part of debris mass is overtopping. Some solid mass is held by the obstacle at $t = 9$ s. The gray patches in the right panels denote the bump in bird's eye view. The arrows in the top panels indicate the flow direction

wave starts from $t > 3$ s. In Fig. 4A, the maximum tsunami height is about 45 m, but in Fig. 3A it was 38 m at $t = 5$ s. Due to the obstacle impact, total impacting debris mass is submerged (or penetrates and is mixed with reservoir) only at $t = 9$ s (left panel f), whereas it was submerged at around $t = 8$ s in the absence of an obstacle (Fig. 3B). The submergence of the impacting debris mass can be recognized by the geometry and position of the solid fraction (on the right panel).

The (maximum) height of the solid component of the debris mixture continuously decreases from 30 m at $t = 0$ s to nearly 10 m at $t = 3$ s (Fig. 4B) and then increases to nearly 19 m at $t = 7$ s, respectively; again it

decreases to a bit more than 12 m at $t = 9$ s. We observe that the maximum solid heights from $t = 3$ s to 7 s in Fig. 4B are larger as compared to those without obstacle in Fig. 3B.

The obstacle holds a portion of the flowing debris mass, and so the solid mass (for a while or permanently). It cannot hold the whole of the decelerated mass in the run-out basin of the reservoir. This is because there is an increase in solid concentration in front of the obstacle. The relative maximum of the solid component is shifted from the inclined part to the front of the obstacle (after $t = 3$ s). Until $t = 5$ s, more solid is held and accumulated at the front of the obstacle. As the pressure associated with the flow depth is increased due to this accumulation, the substantial deflection of the solid occurs resulting in disjoint solid lobes that continue to move forward ($t = 7$ s, panel e, Fig. 4B). These lobes are already strongly elongated in the down-slope direction. We further observe that at $t = 7$ s some solid part is deflected from the lateral sides of the bump forming the parallel downward moving diverging lobes. The maxima of the solid are around the lines $y = \pm 20$ m. At $t = 9$ s, due to the obstacle, a substantial amount of solid mass is still deposited in front of the obstacle. The three interesting phenomena occur simultaneously around the obstacle: a major solid portion is deflected by the obstacle and moves down in two lobes, another small portion tends to overtop the obstacle, and a substantial amount is captured by the obstacle. Due to these multiple effects of flow-obstacle-interaction, there is a substantial loss of kinetic energy, resulting in the decrease in the down-slope motion of the solid in the reservoir (submarine environment).

The maximum solid heights in Fig. 4B are nearly 12 m, 18 m, and 13 m at $t = 5$ s, $t = 7$ s, and $t = 9$ s, respectively. At $t = 9$ s, the maximum heights of the solid mass are at about $x = 240$ m and $x = 230$ m in Figs. 3 and 4, respectively. Thus, even the presence of a single obstacle in the flow path in the reservoir produces a strong disturbance to the forward motion of the debris mass in the reservoir. The travel distance of the frontal solid part is nearly of $x = 295$ m in Fig. 3B, but is only of $x = 275$ m in Fig. 4B. This shortening of the run-out distance shows a substantial energy dissipation. Hence, we conclude that both the amount and speed of the moving mass decrease in the farther downstream as a result of the obstacle impact. Another difference is that the solid mass is totally submerged and mixed with the reservoir (as recognized by the position of the solid mass) nearly at $t = 8$ s in Fig. 4, but it happened to be nearly at $t = 7$ s in Fig. 3. Hence, due to the disturbances created by the obstacle, longer submergence time is taken for debris mass when the reservoir contains an obstacle (Fig. 4) as compared to the case without obstacle (Fig. 3).

B. Bump of height 30 m: Figure 5 describes some basic results as in Fig. 4. But, here, the reservoir contains a bump with increased height of 30 m, which is higher than the height of the water in the reservoir (25 m). The bump has the same radius of 15 m and the center at (220, 0, 0) m as in Fig. 4. As there is no mixture above the bump, the part of the reservoir occupied by the bump appears gray until the mixture height in this vicinity is not higher than 30 m due to impacting debris and induced tsunami. Until $t = 3$ s, the dynamics of the solid and the total height are essentially the same as in Fig. 4. But, after $t = 3$ s, the tsunami amplitude in Fig. 5A is higher in each panel than in Fig. 4A. As the bump is higher than in Fig. 4, more energy is dissipated around the obstacle. This results in the less propagation of water waves downstream than in Fig. 4A. So, the tsunami intensity increases, but the mobility of the tsunamis decreases along with the increasing height of the obstacle. At $t = 5$ s, the strong tsunami wave is seen at the front face of the obstacle, which was much weaker in the previous case. As in the solid, two strong tsunami lobes are induced on either sides of the obstacle already at $t = 5$ s that reunite behind the obstacle later at $t = 7$ s. At $t = 9$ s, these two lobes have coalesced. Such tsunami wave characteristics are not observed in Fig. 4.

At $t = 7$ s, the intensity of the tsunami is higher in Fig. 4A than in Fig. 3A. But, the tsunami intensity is higher in the cross-wise direction in Fig. 5A than in Fig. 4A. This suggests us that the tsunami intensity can be lowered in the downstream direction and can be diverted to the cross-stream direction by increasing the height of the submarine obstacle. Again, the tsunami amplitude is associated with the dynamics of the submarine debris and its impact and depositional (stopping) characteristics of the solid mass around the obstacle. As the bump is higher than in Fig. 4, more solid mass is held and redistributed by the obstacle.

The maximum solid height (see, Fig. 5B) continuously decreases to nearly 10 m at $t = 3$ s due to the spreading, but the maximum solid height rapidly increases to 16 m and 20 m at $t = 5$ s and $t = 7$ s, respectively, and later it decreases nearly to 14 m at $t = 9$ s. But, due to the larger height of the bump, the entire mass is either divided into distributary effluent lobes that travel down-slope or still held by the obstacle. Maximum solid heights from $t = 5$ s to $t \leq 9$ s are substantially larger in this case as compared to the previous case (Fig. 4). At $t = 9$ s, the maximum height of the solid mass is at about 210 m in Fig. 5 which was much farther in Fig. 4. Thus, the presence of the higher obstacle in the flow path in the reservoir produces more disturbance to the forward motion of the solid particle in comparison with its absence or an obstacle of lower height. It shows a substantial energy dissipation due to the impact with higher obstacle (Fig. 5B), and the total

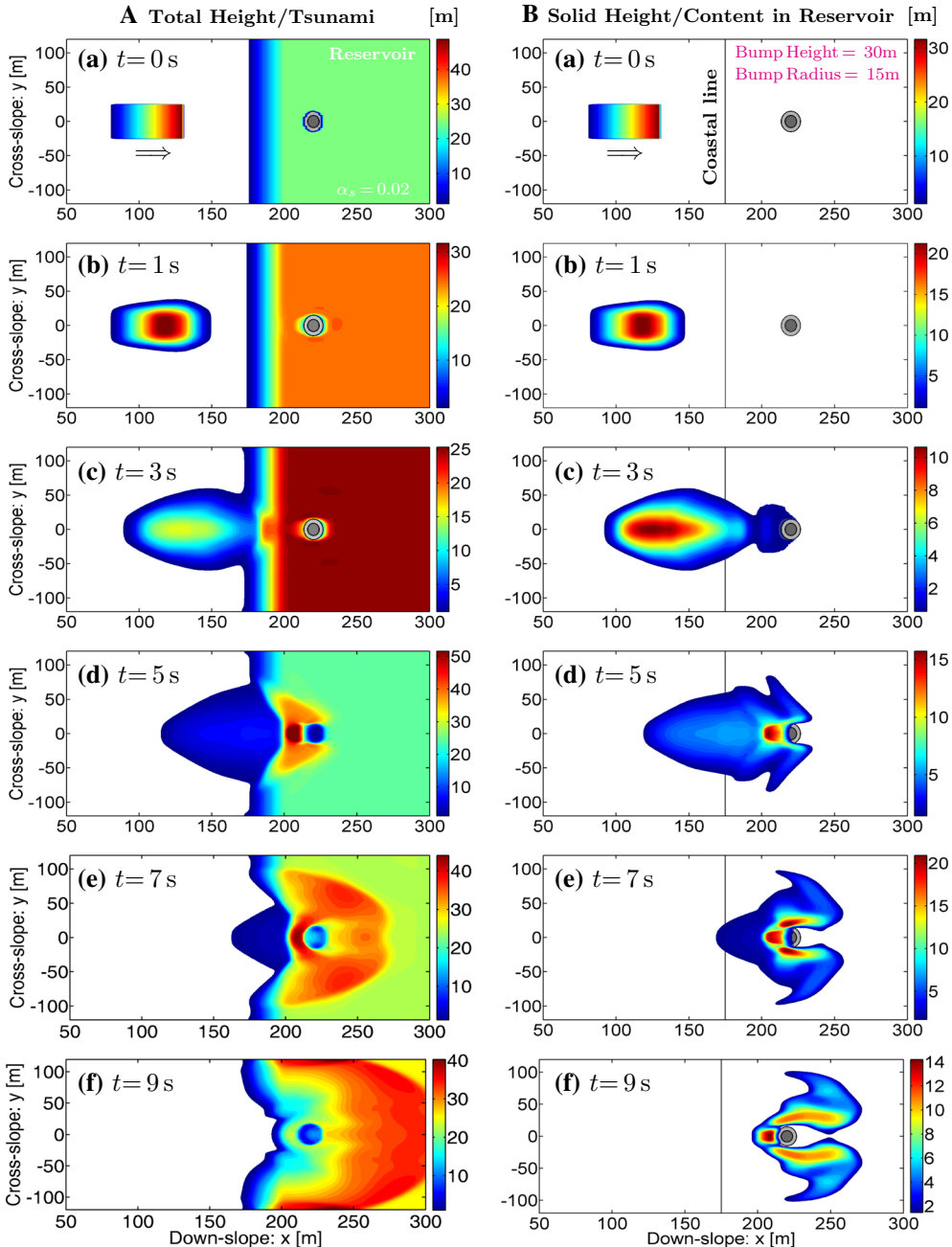


Fig. 5 **A** Total height of the debris mass and tsunamis when initially the reservoir contains a bump of height 30 m as a submarine obstacle with center at (220, 0, 0) m. The intense submarine flow-obstacle-interaction dramatically reduces the flow momentum resulting in the rapid energy dissipation around the obstacle. Tsunami is less mobile here than in previous Figures. **B** Evolution of the solid phase in the debris mixture in the reservoir. Due to the presence of a bump of height 30 m, which is larger than the water height in the reservoir (25 m), the solid part of the debris mass is deflected into two lobes, also a part is captured by the obstacle and no part is overtopping. The gray patch in each panel denotes the bump in bird's eye view. The arrows in the top panels indicate the flow direction

debris mass moves slower down-slope in the reservoir (submarine environment) than in case of the reservoir with lower obstacle (Fig. 4).

II. A bump at different positions

In a natural slope and at its bottom, there may be vegetation or deep rooted and protruding boulders as obstacles. Also, around the run-out region inside the water body, big boulders, islands, and icebergs may be

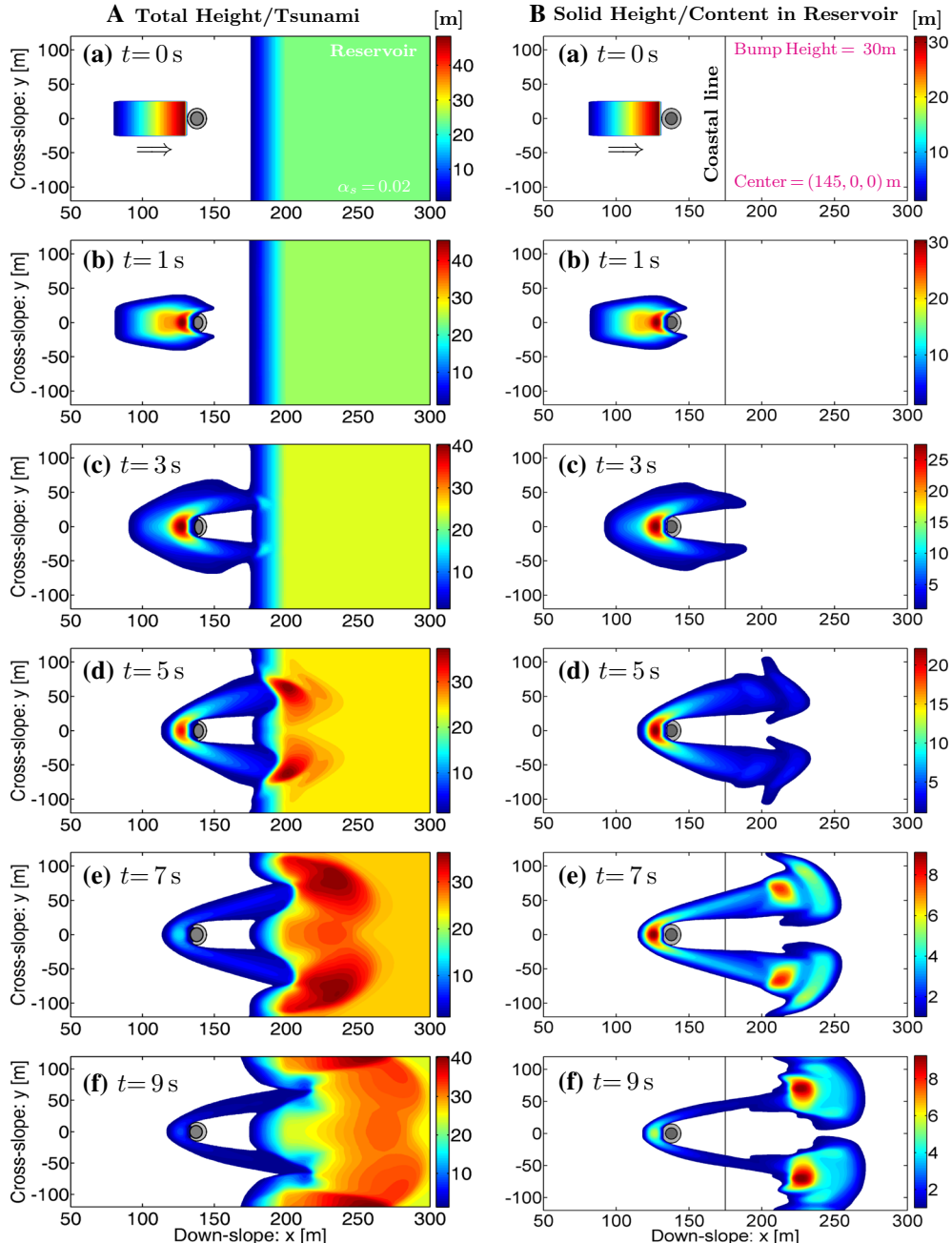


Fig. 6 Bump at the top of subaerial slope. **A** Total height of the debris mass and tsunamis when initially the inclined plane contains a bump as an obstacle with radius 15 m, height 30 m, and center at (145, 0, 0) m. **B** Evolution of the solid phase in the debris mixture in the reservoir. Due to the presence of a bump of height 30 m, both the total debris and the solid component of the debris mass are deflected into two lobes; also a part is captured by the obstacle. The deflection of the solid mass is wider with relative maxima centered nearly at $x = 225$ m. The gray patch in each panel denotes the bump in bird's eye view. The arrows in the top panels indicate the flow direction

found as natural obstacles [52]. To model such possible scenarios, here, we place the obstacles in different positions and analyze in detail the effects of the variation of the bump positions in the down-slope direction. The height and radius of the bump are kept 30 m and 15 m, respectively.

A. Bump touching initial debris mass: Consider a bump that just touches the right end of the initial debris mass (Fig. 6). As soon as the debris is triggered, it impacts the obstacle showing simultaneous piling up of the mass

in front of the obstacle, deflection, redistribution, and branching of the debris material into two lobes. At $t = 1$ s, the maximum of total debris mass decreases slowly to nearly 45 m due to the holding of the debris mass by the bump. As more pressure is developed and the additional gravity force acts, more deflection and spreading occurs, which leads to a further decrease in maximum debris height to 40 m at $t = 3$ s. And, the two deflected debris branches begin to impact the still reservoir. At $t = 5$ s, as streamlined debris lobes continue to impinge on the reservoir, two strong tsunamis are generated and intensified around these two impact regions. At $t = 7$ s, the tsunamis propagate further down-slope and cross-slope, expand and interact to each other, and also with the lateral walls of the reservoir. If we compare it with Fig. 5A, the tsunami, here, travels more cross-slope and less down-slope. The tsunami intensity has very much reduced around the central line (i.e., $y = 0$). But, at this time, the more intense tsunami has propagated toward lateral walls of the reservoir at around $x = 230$ m. At $t = 9$ s, the obstacle is still holding some debris material, but the mass is still flowing down to impinge on the reservoir. The less intense tsunami has traveled farther downstream in the reservoir. Comparing it with Fig. 5, the downstream coastal region can be mitigated more by such placing of an obstacle because the tsunami intensity and mobility have substantially reduced (mainly in the central region of the reservoir). However, relatively higher intensity tsunami waves are found to be localized in both lateral boundary walls due to the confinements.

Next, we analyze the evolution of the solid component of the debris mixture along with the obstacle interaction. At $t = 1$ s, the maximum of solid mass slowly decreases to about 30 m, due to the presence of the obstacle near the initial debris. At $t \geq 1$ s, the obstacle holds the large amount of solid mass and some part is streamlined into two elongated lobes moving down-slope with a maximum height of about 25 m ($t = 3$ s) at the front of the obstacle. As the obstacle is placed much ahead in the upslope, the impacting mass could be held by the obstacle for quite a while, then it moves down-slope, due to gravity and pressure, through two branches, and so the maximum height further decreases to nearly 22 m at $t = 5$ s. The maximum solid position tends to shift from the inclined part to the horizontal region (basin) of the reservoir in the run-out part at $t = 7$ s and begins to show the stopping morphology. There are still laterally strongly curved depositional lobes which are disjoint and contain several local maxima. These morphodynamics are much more complex, and the deflection of solid mass is wider in comparison with the previous simulations. The wider deflection is due to the position of the obstacle nearer to the initial debris mass. The major portion of the solid mass is deposited at around $x = 225$ m at $t = 9$ s. The mass previously captured by the obstacle is still moving continuously down the slope and contributing to amplify and widen the fan in the run-out.

B. Bump at the bottom of the slope: In this case (Fig. 7), until $t = 2$ s, flow dynamics is similar to Fig. 5. As compared to Fig. 6, the tsunami front travels more down-slope and less cross-slope, showing that the tsunami is more mobile. In Fig. 7, the maximum total height is 40 m, but in Fig. 6 it was 37 m at $t = 5$ s. This positioning of the obstacle is important as it produces two laterally oblique water waves of very high intensity ($t = 5$ s) behind the obstacles. These oblique waves begin to merge at $t \geq 5$ s. Thus, we observe that for $t > 3$ s the tsunamis are more intensified as compared to those in Fig. 6 due to the increased distance of the obstacle from the initial debris mass by gaining more velocity due to gravity, and hence the debris mass hits the water in the reservoir with higher impact force. On comparing Figs. 7A and 5A, the total debris flow dynamics and the tsunami generation and propagation differ substantially from $t = 5$ s onward. At $t = 5$ s, the tsunami appears behind the obstacle propagating cross-slope in Fig. 7A, whereas in Fig. 5A it appears in front of the obstacle that persists until $t = 7$ s. In Fig. 7A, the tsunami is propagating more cross-slope.

The solid component of the debris mass in Fig. 7B begins to impact the bump at $t = 3$ s and starts to accumulate at the front of the bump much more than in Fig. 5B. The deflection of the solid into two lobes is more pronounced from $t = 5$ s. Due to the spreading (dispersion) of the solid, its maximum height continuously decreases to nearly 8 m before the flow strikes the bump ($t = 3$ s). The solid mass has dispersed along the cross-slope and down-slope directions so that less height of the debris mass has hit the bump, and thus less solid is captured by the bump than in Fig. 6B. Less mass is diverted in this case as compared to Fig. 6. So, now a narrower deflection of the solid mass occurs that moves farther down-slope. The solid flow dynamics is also different in Figs. 7B and 6B from $t = 3$ s. In Fig. 6B, the major portion of the solid mass is already (momentarily) held by the obstacle, whereas in Fig. 7B only a small portion of the solid mass has approached the obstacle. In Fig. 7B, the major portion of the solid mass is already deflected and diverted at $t = 5$ s, whereas the major portion of the solid mass is still held by the obstacle in Fig. 6. This persists until $t = 9$ s. At $t = 9$ s, the major portion of the solid component forms two fans behind the obstacle in Fig. 7. But, in Fig. 6, the major portion of the solid is in front of the obstacle. The deflected solid lobes are much more longitudinally elongated in Fig. 6 than in Fig. 7. Thus, flow-obstacle-interactions, run-out, and depositional and fan development process are qualitatively similar in early stage, but later there are fundamental differences between Figs. 7 and 6.

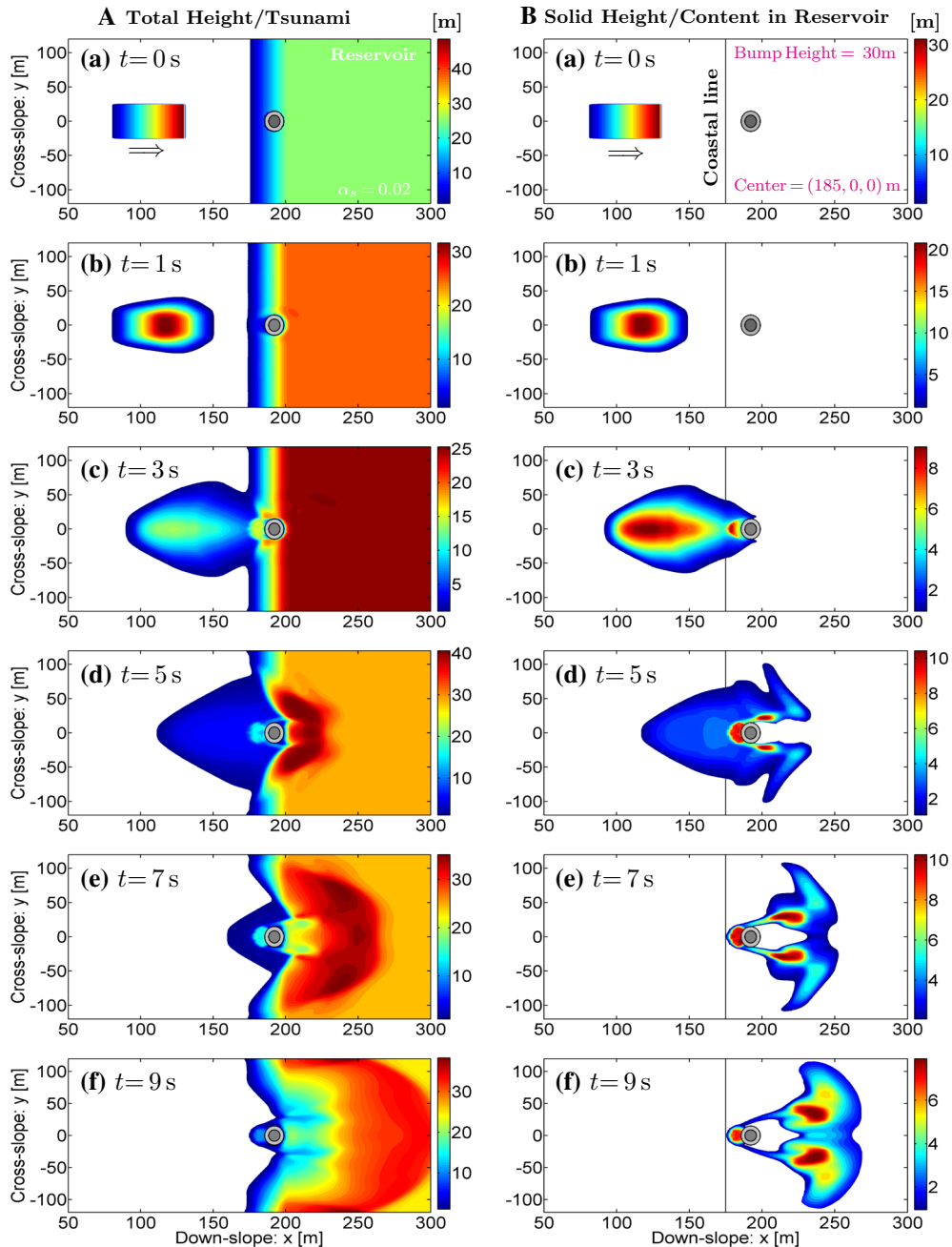


Fig. 7 Bump at the bottom of slope. **A** Total height of the debris mass and tsunamis when initially the reservoir contains a bump as an obstacle with radius 15 m, height 30 m, and at $(185, 0, 0)$ m. **B** Evolution of the solid phase in the debris mixture in the reservoir. Solid part of the debris mass has just started to deflect from $t = 3\text{ s}$ into two branches, and no part is overtopping. Solid mass travels farther down-slope than in Fig. 5. The gray patch in each panel denotes the bump in bird's eye view. The arrows in the top panels indicate the flow direction

C. Bump at the run-out region of the reservoir In Fig. 8, the bump is located at the run-out area. At $t = 5\text{ s}$, the tsunami wave propagates down-slope with the wave head impacting the frontal part of the obstacle. At $t = 7\text{ s}$, the tsunami is more intensified in the vicinity, and remarkably at the front part of the obstacle. At $t = 9\text{ s}$, the tsunami propagates to the lateral banks and the right coast of the reservoir. Maximum energy is dissipated around the obstacle in Fig. 8 mainly at $t = 7\text{ s}$, so that the total height is increased to 43 m.

The changing geometry of the solid component of the debris mass becomes more interesting from $t = 5\text{ s}$ onward. At $t = 5\text{ s}$, there are two maxima of the solid: one just before $x = 200\text{ m}$, and the other more dispersed

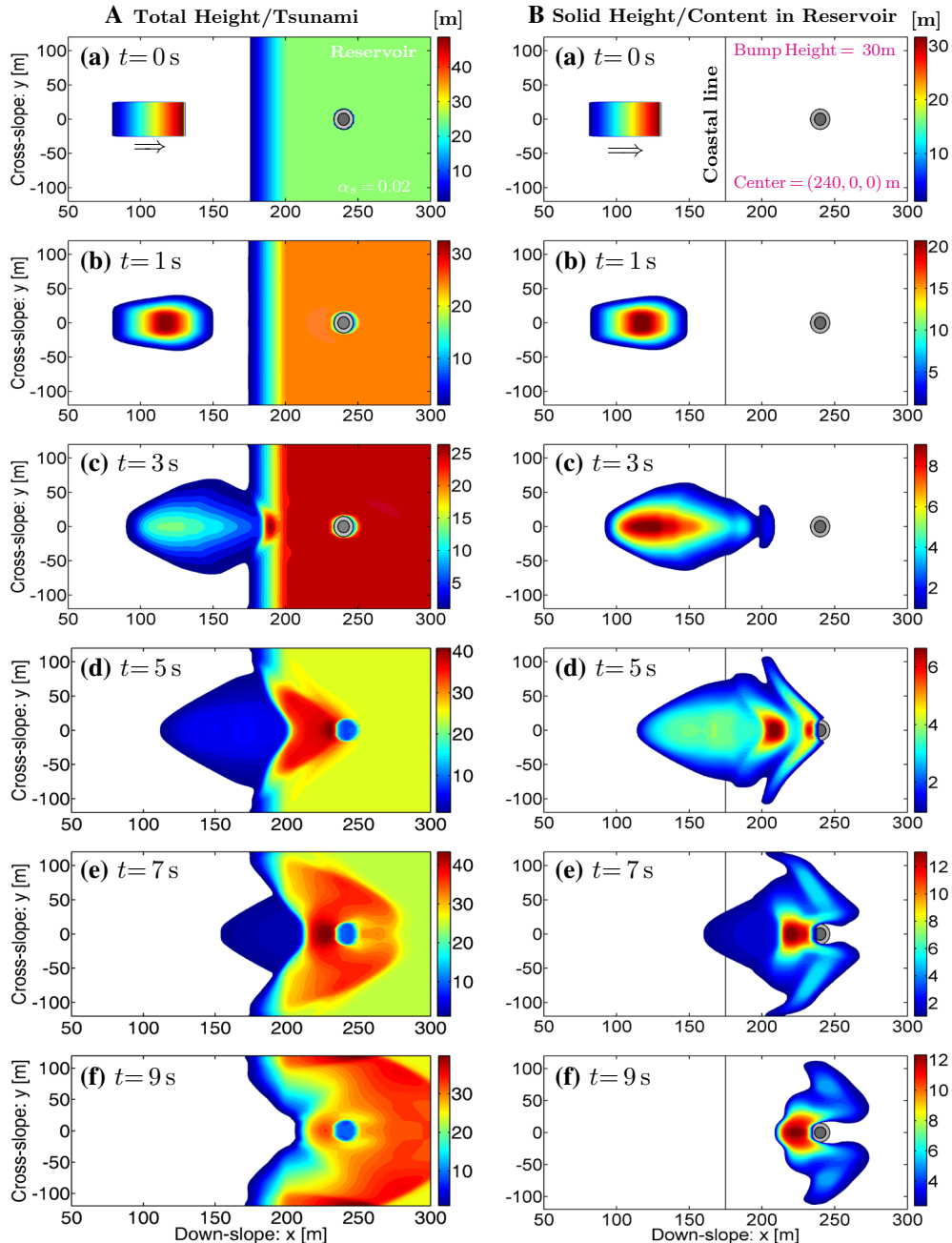


Fig. 8 Bump at the run-out region in the reservoir. **A** Total height of the debris mass and tsunamis when initially the reservoir contains a bump as an obstacle with radius 15 m, height 30 m, and center at (240, 0, 0) m. **B** Evolution of the solid phase in the debris mixture in the reservoir. The solid part of the debris mass has just started to impact the obstacle at about $t = 5$ s. Due to the higher obstacle situated farther down-slope in the run-out zone, the major part of the solid mass is accumulated at the front of the obstacle. The gray patch in each panel denotes the bump position in bird's eye view. The arrows in the top panels indicate the flow direction

maximum around the obstacle front. At $t = 7$ s, the first maximum further moves down-slope and coalesced with the accumulated solid mass in front of the obstacle. Larger accumulation of the solid mass occurs at the front of the obstacle at $t = 7$ s and $t = 9$ s due to the position of the bump at the run-out area, where the substantial deceleration of the mass already took place.

The simulation results presented in Figs. 5, 6, 7, and 8 reveal very interesting dynamics and the obstacle interaction. In Fig. 7, when the bump is kept in the more upstream part of the reservoir basin, a substantial

holding and deflection of the solid mass is observed. The deflection was narrower. In Fig. 8B, the obstacle holds the major portion of the solid. The accumulated solid is more spread, so less in height than in Fig. 5. In Fig. 6, when the obstacle is kept upstream, the solid mass travels less down-slope but is deflected wider. In Fig. 8, when the obstacle is kept farther downstream in run-out, the solid mass travels farther down-slope. Comparison among Figs. 5, 6, 7, and 8 shows fundamentally large differences in the flow-obstacle-interaction, run-out and deposition fan morphodynamics resulting from different positions of the identical obstacle.

Although an obstacle mounted at the subaerial part causes wider deflection in the cross-wise direction than at the submarine part, the placement of the obstacle in the inclined part may be more difficult or may not be feasible. Moreover, the slope stability may be disturbed during the installation of the obstacle at the subaerial part. In addition, the obstacle itself may severely be damaged, causing more destruction. However if the slope is less steep, or placing of obstacles in the submarine part is less feasible due to the safety reasons, the mounting of obstacles in the subaerial part can be useful.

3.3.3 Effects of multiple bumps

Instead of a single larger obstacle, often in practice integrated obstacles of smaller sizes are installed to achieve more effective obstacle interaction, flow dispersion, and momentum dissipation [24, 32, 54]. So, we present further simulations which are performed with integrated bumps of different radii, different numbers and positions.

I. All bumps in the reservoir

Simulations are performed with the reservoir containing five bumps of different sizes as two series of (expanding radially outward) submarine obstacles (Fig. 9). We have chosen the radius of the bumps smaller in downstream as they will be impacted by a less amount of diverted debris lobes with reduced speed. Due to the presence of the increased number of obstacles in the reservoir, a tsunami with less mobility is produced as compared to Figs. 3, 4 and 5.

As the debris mass impacts the following obstacles, this reduces the flow speed which results in substantial increase of the tsunami amplitudes. The velocities of tsunamis, as inferred from the front position, are less in Fig. 9 than those in the previous cases (Figs. 3, 5). Tsunami amplification dynamics is more complex with multiple waves now. In Fig. 9, the maximum total height slowly decreases from nearly 53 m at $t = 5$ s to 50 m at $t = 7$ s, but in Fig. 5 it rapidly decreases from 51 m at $t = 5$ s to 43 m at $t = 7$ s. This is because there is more disturbance in the flow due to the impact with multiple bumps in the reservoir and the holding of mass between them. We observed that the tsunami is less mobile when we increase the number of obstacles in the reservoir as compared to the single obstacle (Fig. 5) and without obstacle (Fig. 3).

In Fig. 9B, the maximum solid height is nearly 18 m and 24 m at $t = 5$ s and $t = 7$ s, respectively, and then decreases again to 18 m at $t = 9$ s. The solid mass separates into two longitudinal branches from $t > 3$ s, and then each of these branches is deflected and divided again into two sub-branches by the other two following obstacles from $t > 5$ s, and each is again separated (sub-divided) into further two sub-branches from $t = 7$ s. This resulted in a total of six lobes ($t = 9$ s). We clearly observe that the major portion of the solid mass has been held in front, and in between the obstacles, in five different positions, so that the moving mass decreases in both amount and speed as compared to previous Figures. At $t = 9$ s, the frontal solid surges reach a down-slope distance of $x = 259$ m in Fig. 9B. But, they reach much farther in Fig. 5B and even farther in Fig. 4B (see Table 2). This clearly shows that when we increase the number of obstacles on the bathymetric surface placed in an obliquely expanding sequence, we can deflect and redirect more of the mass flow enabling to decrease the adverse effect of debris impact and tsunami.

Since each obstacle divides the solid mass into two lobes, fingering and meandering multiple streamed lobes are observed as the solid mass moves down-slope. A significant amount of solid mass is stopped by the system of obstacles. The system of obstacles creates much higher intensity tsunamis. The less mobility of the tsunami and turbidity current result from the much more dissipation of energy during multiple impacts. Hence, constructing appropriate obstacles in different numbers and dimensions installed at different bathymetric positions is an important coastal engineering solution to the submarine mass flow and tsunami hazards.

II. All bumps in subaerial slope

Finally, simulations are performed with five bumps all placed on the subaerial slope (Fig. 10). For $t = 1$ s, the dynamics is similar to Fig. 6. At $t \geq 3$ s, the multiple streamed debris lobes already hit the left coast of the reservoir, and the tsunamis are generated. As the debris lobes continue to hit across the reservoir, the tsunami intensifies also in cross-wise directions and propagates both in down-slope and cross-slope directions ($t = 7$ s). The tsunami reaches only at a downstream distance of about $x = 265$ m at $t = 9$ s. This is mainly due to the

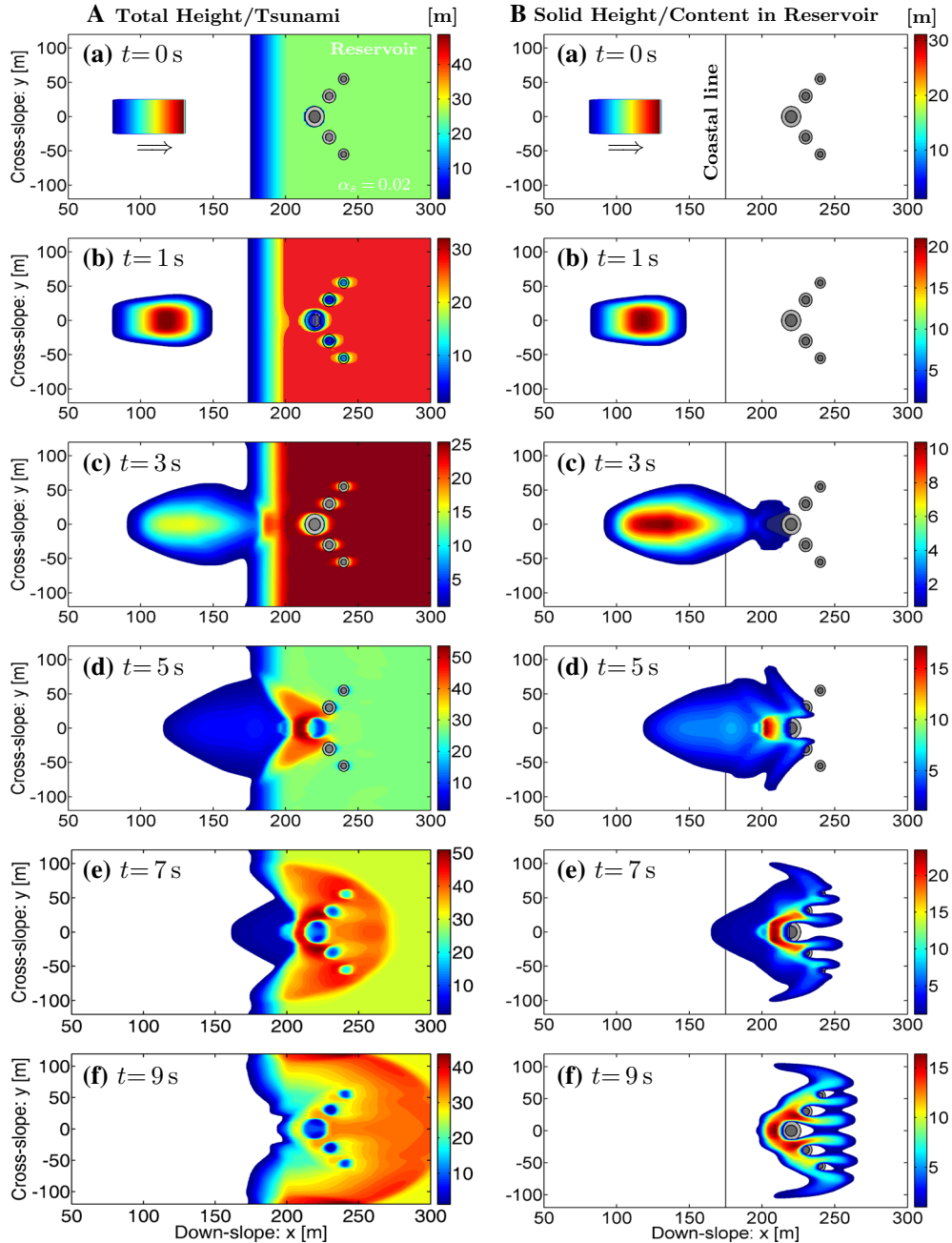


Fig. 9 All bumps in submarine environment. **A** Total height of the debris mass and tsunamis when initially the reservoir contains a bump as an obstacle with radius 15 m, height 30 m, and center at $(220, 0, 0)$ m which is followed by two bumps having smaller radii of 10 m at $(230, \pm 30, 0)$ m, again which are followed by two other bumps having even smaller radii of 8 m at $(240, \pm 55, 0)$ m. **B** Evolution of the solid phase in the debris mixture in the reservoir. Multiple obstacles reduce the tsunami and submarine landslide mobility more as compared to the single obstacle in a reservoir and a reservoir without obstacle. The gray patches in each panel denote the bumps in bird's eye view. The arrows in the top panels indicate the flow direction

deceleration of the debris mass by the system of obstacles, and also by the impact of multiple debris lobes on the coast of the reservoir.

Until $t = 1\text{ s}$, flow dynamics of the solid phase is similar to Fig. 6. Afterward, each branch of the solid mass is further divided into two sub-branches. The branches are further elongated. At $t = 9\text{ s}$, the maximum solid position is continuously shifted from the inclined to the run-out part while passing through the five obstacles,

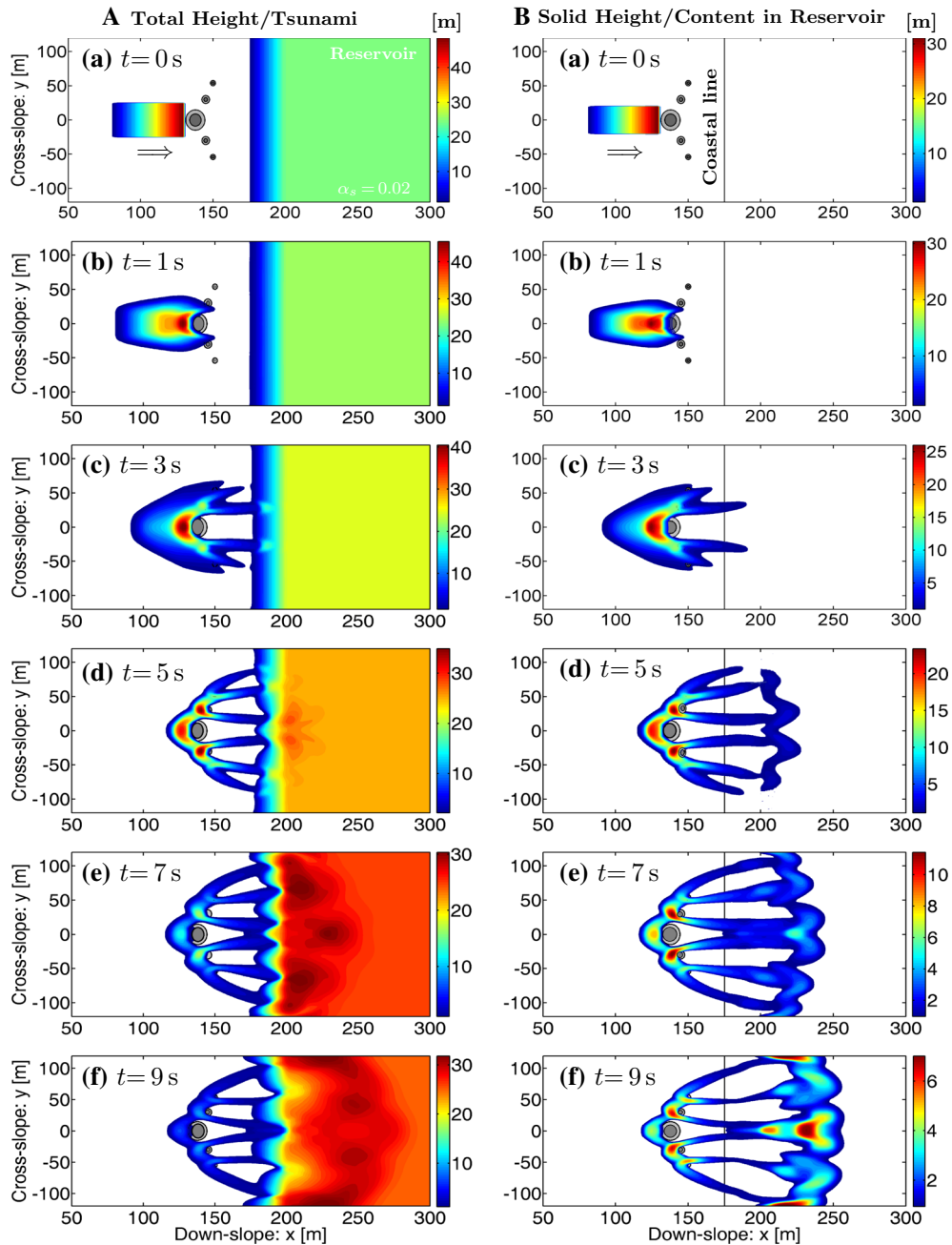


Fig. 10 All bumps in subaerial slope. **A** Total height of the debris mass and tsunamis when a bump is a subaerial obstacle with radius 15 m, height 30 m, and center at (135, 0, 0) m which is followed by two bumps having the same radii of 8 m at (140, ± 30 , 0) m, again which are followed by two other bumps having the same radii 6 m and at (145, ± 55 , 0) m are mounted in subaerial slope. **B** Evolution of the solid phase in the debris mixture in the reservoir. As all the obstacles are in subaerial slope, the deflection is wider. The tsunami is less mobile and more intensified at left and right banks of the reservoir. The gray patches in each panel denote the bumps in bird's eye view. The arrows in the top panels indicate the flow direction

but the solid maxima are divided into several local maxima either in between the obstacles, at the central part of the run-out area, or near the lateral walls of the reservoir.

It is interesting to observe that the tsunami and the mass movement in the reservoir and the mass halting (deposition) pattern are different from those in Fig. 6. Due to the coalescence of the central streaming lobes in the run-out plane, the main depositional lobe induced by mass stopping is developed in the center for the solid, while the tsunami wave is maximum here ($t = 7$ s). The tsunami intensity at this location is less than that in

Table 1 Comparison of tsunami amplitudes and tsunami front positions for different obstacle configurations at time $t = 7$ s

| Obstacles configurations | | Tsunami amplitude | | Tsunami front position | |
|--|------------|-------------------|-------------------|------------------------|-------------------|
| Simulation type | Index: i | (A_i) (m) | $\frac{A_i}{A_0}$ | (x_i) (m) | $\frac{x_i}{x_0}$ |
| No obstacle (Fig. 3A) | 0 | 13 ($= A_0$) | 1 | 295 ($= x_0$) | 1 |
| Bump of height 15 m (Fig. 4A) | 1 | 15 | 1.153 | 290 | 0.983 |
| Bump of height 30 m (Fig. 5A) | 2 | 20 | 1.538 | 280 | 0.949 |
| Bump touching initial mass (Fig. 6A) | 3 | 11 | 0.846 | 263 | 0.891 |
| Bump at bottom of slope (Fig. 7A) | 4 | 10 | 0.769 | 270 | 0.915 |
| Bump at run-out region (Fig. 8A) | 5 | 18 | 1.384 | 280 | 0.949 |
| Multiple bumps in reservoir (Fig. 9A) | 6 | 25 | 1.923 | 265 | 0.898 |
| Multiple bumps in subaerial slope (Fig. 10A) | 7 | 5.5 | 0.423 | 245 | 0.830 |

Fig. 6, but it forms strong patterns; local tsunami wave pockets, interaction, expansion, and reflection can be seen at $t \geq 5$ s. This choice of obstacle system makes the submarine particle flow less mobile and localized at different positions in the reservoir. There is a wider deflection of the solid mass in Fig. 10 than in Fig. 9, resulting in smaller travel distance. So, the obstacles in the subaerial part make the tsunami less mobile than placing the obstacles in submarine part, thereby decreasing the inundation area.

The fundamentally completely different dynamics, run-out, and stopping behaviors of the tsunami and (submarine) mass movements in the reservoir associated with flow-obstacle-interaction reveal very important features of two-phase mass flows. In the past, largely single-phase landslide impacting a water reservoir has been simulated by artificially coupling the simulation of granular-type landslide motion to shallow water motion of the water in the reservoir in which the coupling is done only by adding the landslide (submerged) height to the height of water that artificially generates water waves with amplification in proportion of the submerged landslide, so just coupled by external pushing of the water body [5, 50, 67, 74]. For this type of classical flow simulation, at least for short time, the dynamics of the submerged mass and the surface water waves are similar, but we have shown (Fig. 10, $t = 9$ s) that it is not realistic because maximum of the solid mass in the reservoir and the maximum of the tsunami do not necessarily take place at the same location. So, our model and simulation are important contributions to the submarine (landslide) and submarine morphodynamics.

3.3.4 Comparisons of tsunami amplitudes and run-out scenarios

Now, we discuss the change in tsunami amplitudes and run-out scenarios of the different results in Figs. 3, 4, 5, 6, 7, 8, 9, and 10. As high-intensity tsunamis are observed in $t = 7$ s in almost all cases, we compare the amplitudes (A_i) of the tsunamis at this time (see Table 1). In the reference simulation when there is no obstacle, the highest tsunami amplitude (at around $x = 250$ m) was of $A_0 = 13$ m. When the obstacles are mounted in the reservoir, the tsunami amplitude increases, whereas the amplitude decreases when the obstacles are mounted on subaerial slope, i.e., $A_3, A_4, A_7 < A_0$ and $A_1, A_2, A_5, A_6 > A_0$. The tsunami amplitude increases with increasing obstacle height ($A_2 > A_1$). In Fig. 9A, when there are multiple bumps in the reservoir, the amplitude increases by nearly $((25 - 13)/13) \times 100\% = 92\%$, whereas in Fig. 10A when there are multiple bumps in the subaerial slope, the tsunami amplitude decreases by nearly $((13 - 5.5)/13) \times 100\% = 57\%$ on comparing with the reference simulation without obstacle (Fig. 3). In fact, when the multiple bumps were in the reservoir (Fig. 9), the obstacle impact of the flow with higher momentum and kinetic energy produced higher tsunami intensity. This was due to the multiple obstruction induced amplified tsunamis. But, the flow is already divided into multiple lobes and there was larger energy dissipation during obstacle impact in the subaerial slope (Fig. 10). The divided lobes with lower momentum and kinetic energy create waves of lower intensity. The comparisons for other obstacle configurations with the no obstacle case are listed in Table 1 under the column A_i/A_0 .

Similarly, we compare the front position (x_i) of the tsunamis in Table 1 for $t = 7$ s. The column x_i/x_0 of Table 1 shows that each obstacle configuration is responsible for substantially shortening of tsunami wave propagation, but in a different way than that without obstacle. The down-slope propagation of the tsunami wave decreases with increasing obstacle height and number (i.e., $x_2, x_6 < x_1$). The debris mass is substantially decelerated with the bump touching the initial debris mass at the subaerial slope (Fig. 6). The two decelerated and redirected debris lobes hit the water surface with less impact force. The tsunami propagates less down-slope; a tsunami with higher intensity can be seen near the lateral walls of the reservoir. The least extent of propagation is seen in Fig. 10A, when there are multiple bumps in the subaerial slope. In fact, with multiple

Table 2 Comparison of maximum solid height and solid front positions in case of different obstacle configurations at time $t = 9$ s

| Obstacles configurations | | Maximum solid height | | Solid front position | |
|--|------------|----------------------|-------------------|----------------------|-------------------|
| Simulation type | Index: i | (M_i) (m) | $\frac{M_i}{M_0}$ | (x_i) (m) | $\frac{x_i}{x_0}$ |
| No obstacle (Fig. 3B) | 0 | 13 ($= M_0$) | 1 | 295 ($= x_0$) | 1 |
| Bump of height 15 m (Fig. 4B) | 1 | 12.5 | 0.961 | 275 | 0.932 |
| Bump of height 30 m (Fig. 5B) | 2 | 14 | 1.076 | 268 | 0.908 |
| Bump touching initial mass (Fig. 6B) | 3 | 9 | 0.692 | 258 | 0.874 |
| Bump at bottom of slope (Fig. 7B) | 4 | 7.5 | 0.576 | 260 | 0.881 |
| Bump at run-out region (Fig. 8B) | 5 | 12 | 0.923 | 272 | 0.922 |
| Multiple bumps in reservoir (Fig. 9B) | 6 | 17 | 1.307 | 259 | 0.878 |
| Multiple bumps in subaerial slope (Fig. 10B) | 7 | 7 | 0.538 | 255 | 0.864 |

bumps in the reservoir (Fig. 9), both the impact of the highly accelerated debris mass at the reservoir and the energy dissipation around multiple obstacles produce the tsunami of highest intensity.

It is interesting to compare the maxima and the front positions of the solid content or the submarine flow scenarios and their run-out patterns at $t = 9$ s. Table 2 presents the detailed quantitative description of the maximum solid depth and the front position and their comparisons with the reference simulation (no obstacle, Fig. 3B). When there is no obstacle (Fig. 3), the maximum solid mass gets accumulated at the central part of the reservoir. When the obstacle is placed at the front part of the run-out zone in the reservoir (Fig. 8), a substantial solid mass is held by the obstacle and another part of the solid mass is deflected in two elongated lobes, so $M_1 < M_0$. Since the increase in obstacle height increases the solid mass accumulation in the vicinity of the obstacle, we observed that $M_2 > M_1, M_0$. With the obstacle in subaerial slope (Fig. 6), the solid mass was diverted into two lobes with the local maxima a bit farther downstream in the reservoir. So, $M_3 < M_0, M_1, M_2$. When the bump is placed at the bottom of the inclined part in the reservoir (Fig. 7), the debris mass is less diverted cross-wise. The position of the relative maxima is a bit farther down-slope as compared to Fig. 6 (i.e., $x_3 < x_4$). It is even more interesting to compare the run-out scenario of Fig. 7 with Fig. 5 as the relative maximum travels farther down-slope in Fig. 7, because more solid mass is held by the obstacle in Fig. 5. In Fig. 8, when a single bump is placed at the run-out area of the reservoir, the bump holds the major portion of the solid at its frontal part. As the maximum is more dispersed than in Fig. 3 (no obstacle), the maximum of the solid content is less here. Finally, in Fig. 10, when the system of five obstacles is mounted in the subaerial slope, the solid mass is accumulated not only at the run-out area, but also in between the obstacles. As the accumulation of the solid mass is localized in many different parts of the flow domain, the maximum solid depth decreases drastically here as compared to Fig. 9 (multiple bumps at the submarine part). Thus, the obstacle height, position and number play a crucial role in the tsunami intensity, front position, and submarine mass accumulations and movement.

The simulation results show that in subaerial and submarine environments flow-obstacle-interactions drastically reduce the flow momentum resulting in the rapid energy dissipation around obstacles. When we increase the height of the obstacle in the submarine environment, more solid mass is captured and redistributed, more energy is dissipated around the obstacle, and hence tsunami is less mobile so that the tsunami is less hazardous in the downstream. Therefore, placing an obstacle in the flow path controls the flow dynamics by reducing the destructive wave impact, run-up and the resulting damages. Changing the position of obstacles brings a substantial change in the flow dynamics, mainly in holding of mass, its deflection, redirection, and the resulting tsunami intensity and run-ups. The increased number of obstacles magnifies this effect, and the moving mass decreases in both amount and speed. Thus, submarine obstacles can be useful for the prevention and mitigation of the tsunami hazard and submarine mass movements to the coastal and mountain population and infrastructures. Another important observation is the run-out morphodynamics and flow stopping which is strongly controlled by submarine obstacles. If the impact force is high enough, the tsunami intensity increases due to the impact; submarine objects in the water body may be damaged. Such damage can be minimized by reducing the kinetic energy of the flow by placing appropriate obstacles in the upstream.

In order to substantially mitigate mountain and coastal hazards, and the integrity of hydraulic power plants, it is important to properly understand submarine landslide and tsunami interactions with submarine obstacles. Our findings contribute significantly to our understanding of mixing and separation between phases, generation, and propagation of special solid and fluid structures, and transitions during the flow process. By properly translating the mountain topography, the obstacle geometry and the reservoir to the real field physical settings by our modeling and computational techniques, the magnitudes and run-ups of possible tsunamis, sediment

transport in water bodies, and the change of the intensity of the tsunami by the obstacles can be described. This can be useful for prevention and mitigation plans.

4 Summary

The general two-phase physical–mathematical mass flow model [60] is solved numerically by applying a high-resolution shock-capturing numerical scheme for two-phase landslide and its impact on reservoir, interaction with the obstacles and the associated tsunamis and submarine mass flows. The formation, amplification, propagation, reflection, and intersection of coupled tsunami waves are observed as a subaerial two-phase landslide impacts the quiescent water reservoir with or without obstacle.

Although our model and simulation techniques could not explicitly distinguish between the submerged landslide and upper water layer, we could include dynamic interaction of evolving solid and fluid phases with strong interfacial momentum transfer for the mixing at the landslide-water interface, along with the inclusion of Newtonian and non-Newtonian viscous stresses, which the existing models ignore. Due to the presence of an obstacle, the intense flow-obstacle-interaction drastically reduces the flow momentum resulting in the rapid energy dissipation around the obstacle, and the resulting tsunami is less mobile in down-slope direction than with no obstacle as the obstacle can catch, deflect, redirect or redistribute some portion of the landslide mass. The tsunami produced in the vicinity of the obstacle during the impact propagates both down-slope and cross-slope. Obstacles in the flow path influence the flow dynamics by reducing the destructive impact, run-up, and the resulting damages. When the height of the obstacle is increased, less or no solid mass is overtapped. This results in the increased holding or deflection of the solid mass by the obstacle. Tsunamis with higher amplitudes are produced with more obstacles in comparison with less or no obstacle in the reservoir as they create more disturbances to the motion of the fluid and landslide in the reservoir. The moving mass decreases in both amount and speed since each obstacle impacts the flow to deflect the main flowing mass into two streams and also to capture a portion of it, which is very important to decrease the landslide and tsunami effects. The placing of obstacles at different positions in subaerial slope and in the base of the reservoir significantly affects the tsunami intensity, the obstacle interaction, energy dissipation, and overall flow dynamics. The obstacles mounted in the subaerial slope create a less mobile tsunami than those mounted down in the reservoir. When the obstacles are installed more upstream on the subaerial slope, the deflection is wider with less holding of landslide/debris mass. These novel observations help us for the proper understanding of landslide and debris induced tsunamis in mountain lakes, channels, and reservoirs containing obstacles of different sizes, positions and number in subaerial and submarine environments, the associated dynamics of turbidity current, sediment transport, and submarine landslides. These results may be extended and applied to hazard mitigation, prevention, and solving relevant engineering or environmental problems.

Acknowledgements We thank the Editor Professor Cristian Marchioli and reviewers for their constructive comments that helped to improve the manuscript substantially. We gratefully acknowledge the financial support provided by the German Research Foundation (DFG), by the research projects, PU 386/3-1:“Development of a GIS-based Open Source Simulation Tool for modeling General Avalanche and Debris Flows over Natural Topography” and PU 386/5-1: “A novel and unified solution to multi-phase mass flows”: U_MultiSol. Parameshwari Kattel acknowledges University Grants Commission (UGC), Nepal, for the financial support provided as a PhD fellowship (PhD-2071/072-Sci. & Tech.-03).

References

1. Abadie, S., Morichon, D., Grilli, S., Glockner, S.: Numerical simulation of waves generated by landslides using a multiple-fluid Navier–Stokes model. *Coast. Eng.* **57**(9), 779–794 (2010)
2. Awal, R., Nakagawa, H., Fujita, M., Kawaike, K., Baba, Y., Zhang, H.: Experimental study on glacial lake outburst floods due to waves overtopping and erosion of moraine dam. *Annu. Disaster Prev. Res. Inst. Kyoto Univ.* **53B**, 583–594 (2010)
3. Breien, H., De Bakker, F.V., Elverhoi, A., Hoeg, K.: Erosion and morphology of a debris flow caused by a glacial lake outburst flood. *Western Norway. Landslides* (2008). <https://doi.org/10.1007/s10346-008-0118-3>
4. Bout, B., Lombardo, L., van Westen, C.J., Jetten, V.G.: Integration of two-phase solid fluid equations in a catchment model for flashfloods, debris flows and shallow slope failures. *Environ. Model. Softw.* **105**, 1–16 (2018). <https://doi.org/10.1016/j.envsoft.2018.03.017>
5. Cecioni, C.: Numerical Modeling of Waves for a Tsunami Early Warning System. PhD Dissertation, University Degli Studi ROMA TRE (2010)
6. Cui, X., Gray, J.M.N.T.: Gravity-driven granular free-surface flow around a circular cylinder. *J. Fluid Mech.* **720**, 314–337 (2013). <https://doi.org/10.1017/jfm.2013.42>

7. Domnik, B., Pudasaini, S.P., Katzenbach, R., Miller, S.A.: Coupling of full two-dimensional and depth-averaged models for granular flows. *J. Non Newton. Fluid Mech.* **201**, 56–68 (2013)
8. Douglas, S.: Numerical Modeling of Extreme Hydrodynamic Loading and Pneumatic Long Wave Generation: Application of a Multiphase Fluid Model. PhD Dissertation, University of Ottawa, Canada (2016)
9. Faug, T., Gauer, P., Lied, K., Naaim, M.: About observations of the overrun length of avalanches overtopping catching dams: cross-comparison of small scale laboratory experiments and observations from full-scale avalanches. *J. Geophys. Res.* (2008). <https://doi.org/10.1029/2007JF000854>
10. Faug, T., Chanut, B., Beguin, R., Naaim, M., Thibert, E., Baraudi, D.: A simple analytical model for pressure on obstacles induced by snow avalanches. *Ann. Glaciol.* **51**(54), 1–8 (2010)
11. Faug, T.: Depth-averaged analytic solutions for free-surface granular flows impacting rigid walls down inclines. *Phys. Rev. E* (2015). <https://doi.org/10.1103/PhysRevE.92.062310>
12. Fischer, J.-T., Kowalski, J., Pudasaini, S.P.: Topographic curvature effects in applied avalanche modeling. *Cold Reg. Sci. Technol.* **74–75**, 21–30 (2012)
13. Fridman, A.M., Alprovich, L.S., Shemer, A.L., Pustil'nik, L., Shtivelman, D., Marchuk, A.G., Liberzon, D.: Tsunami wave suppression using submarine barriers. *Phys. Uspekhi* **53**(8), 843–850 (2010)
14. Fritz, H.M.: Initial Phase of Landslide Generated Impulse Waves. PhD Dissertation, Swiss Federal Institute of Technology, ETH Zürich, Switzerland (2002)
15. Fritz, H.M., Hager, W.H., Minor, H.-E.: Landslide generated impulse waves. 2. Hydrodynamic impact craters. *Exp. Fluids* **35**, 520–532 (2003). <https://doi.org/10.1007/s00348-003-0660-7>
16. Fritz, H.M., Hager, W.H., Minor, H.-E.: Near field characteristics of landslide generated impulse waves. *J. Waterw. Port Coast. Ocean Eng.* **130**(6), 287–302 (2004). [https://doi.org/10.1061/\(ASCE\)0733-950X](https://doi.org/10.1061/(ASCE)0733-950X)
17. Glimsdal, S., Pedersen, G.K., Harbitz, C.B., Lovholt, F.: Dispersion of tsunamis: does it really matter? *Nat. Hazards Earth Syst. Sci.* **13**, 1507–1526 (2013). <https://doi.org/10.5194/nhess-13-1507-2013>
18. Gray, J.M.N.T.: Granular flow in partially filled slowly rotating drums. *J. Fluid Mech.* **441**, 1–29 (2001)
19. Gray, J.M.N.T., Tai, Y.-C., Noella, S.: Shock waves, dead zones and particle-free regions in rapid granular free-surface flows. *J. Fluid Mech.* **491**, 161–181 (2003). <https://doi.org/10.1017/S0022112003005317>
20. Grilli, S.T., Vogelmann, S., Watts, P.: Development of a 3D numerical wave tank for modeling tsunami generation by underwater landslides. *Eng. Anal. Bound. Elem.* **26**(4), 301–313 (2002)
21. Grilli, S.T., Ioualalen, M., Asavanant, J., Shi, F., Kirby, J., Watts, P.: Source constraints and model simulation of the December 26, 2004, Indian Ocean tsunami. *J. Waterw. Port Coast. Ocean Eng.* **133**, 414–428 (2007)
22. Grilli, S.T., O'Reilly, C., Harris, J.C., Bakhsh, T.T., Tehranirad, B., Banihashemi, S., Kirby, J.T., Baxtar, C.D.P., Eggeling, T., Ma, G., Shi, F.: Modeling of SMF tsunami hazard along the upper US East Coast: detailed impact around Ocean City, MD. *Nat. Hazards* **76**(2), 705–746 (2015)
23. Grilli, S.T., Shelby, M., Kimmoun, O., Dupont, G., Nicolsky, D., Ma, G., Kirby, J.T., Shi, F.: Modeling coastal tsunami hazard from submarine mass failures: effect of slide rheology, experimental validation, and case studies off the US East Coast. *Nat. Hazards* **86**(1), 353–391 (2017)
24. Hákonardóttir, K.M., Hogg, A.J., Jóhannesson, T., Tomasson, G.G.: A laboratory study of the retarding effects of braking mounds on snow avalanches. *J. Glaciol.* **49**(165), 191–200 (2003)
25. Hampton, M.A., Lee, H.J., Locat, J.: Submarine landslides. *Rev. Geophys.* **34**, 33–59 (1996)
26. Haugen, K.B., Lovholt, F., Harbitz, C.B.: Fundamental mechanisms for tsunami generation by submarine mass flows in idealised geometries. *Mar. Petrol. Geol.* **22**(1–2), 209–217 (2005)
27. Heinrich, P.: Nonlinear water waves generated by submarine and aerial landslides. *J. Waterw. Port Coast. Ocean Eng.* **118**, 249–266 (1992)
28. Heinrich, P., Piatanesi, A., Hebert, H.: Numerical modelling of tsunami generation and propagation from submarine slumps: the 1998 Papua New Guinea events. *Geophys. J. Int.* **145**, 97–111 (2001)
29. Iverson, R.M.: The physics of debris flows. *Rev. Geo Phys.* **35**(3), 245–296 (1997)
30. Iverson, R.M., Denlinger, R.P.: Flow of variably fluidized granular masses across three-dimensional terrain: 1. Coulomb mixture theory. *J. Geophys. Res.* **106**(B1), 537–552 (2001)
31. Jiang, L., LeBlond, P.H.: Numerical modeling of an underwater Bingham plastic mudslide and the waves which it generates. *J. Geophys. Res.* **98**(C6), 10303–10317 (1993). <https://doi.org/10.1029/93JC00393>
32. Jóhannesson, T., Gauer, P., Issler, D., Lied, K.: The design of avalanche protection dams. Recent practical and theoretical developments. European Commission. Directorate General for Research (Barbolini M, Domaas U, Harbitz CB, Johannesson T, Gauer P, Issler D, Lied K, Faug T, Naaim M) (2009)
33. Kafle, J., Pokhrel, P.R., Khattri, K.B., Kattel, P., Tuladhar, B.M., Pudasaini, S.P.: Landslide-generated tsunami and particle transport in mountain lakes and reservoirs. *Ann. Glaciol.* **57**(71), 232–244 (2016). <https://doi.org/10.3189/2016AoG71A034>
34. Kattel, P., Khattri, K.B., Pokhrel, P.R., Kafle, J., Tuladhar, B.M., Pudasaini, S.P.: Simulating glacial lake outburst floods with a two-phase mass flow model. *Ann. Glaciol.* **57**(71), 349–358 (2016). <https://doi.org/10.3189/2016AoG71A039>
35. Kattel, P., Kafle, J., Fischer, J.-T., Mergili, M., Tuladhar, B.M., Pudasaini, S.P.: Interaction of two-phase debris flow with obstacles. *Eng. Geol.* **217**, 197–242 (2018). <https://doi.org/10.1016/j.enggeo.2018.05.023>
36. Kim, G.-B.: Numerical Simulation of Three-Dimensional Tsunami Generation by Subaerial Landslides. Master's Thesis, Texas A&M University, Texas, USA (2012)
37. Kirby, J.T., Shi, F., Nicolsky, D., Misra, S.: The 27 April 1975 Kitimat, British Columbia, submarine landslide tsunami: a comparison of modeling approaches. *Landslides* **13**(6), 1421–1434 (2016)
38. Lecomte, I., Thollet, I., Juliussen, H., Hamran, S.E.: Using geophysics on a terminal moraine damming a glacial lake: the Flatbre debris flow case, Western Norway. *Adv. Geosci.* **14**, 301–307 (2008)
39. Legros, F.: The mobility of long-run out landslides. *Eng. Geol.* **63**(3–4), 301–331 (2002)
40. Liu, J.F., Mauzerall, D.L., Horowitz, L.W.: Analysis of seasonal and interannual variability in transpacific transport. *J. Geophys. Res. Atmos.* (2005). <https://doi.org/10.1029/2004JD005207>

41. Lovholt, F., Pedersen, G., Harbitz, C.B., Glimsdal, S., Kim, J.: On the characteristics of landslide tsunamis. *Philos. Trans. R. Soc. A* **373**, 20140376 (2015). <https://doi.org/10.1098/rsta.2014.0376>
42. Ma, G., Shi, F., Kirby, J.T.: Shock-capturing non-hydrostatic model for fully dispersive surface wave processes. *Ocean Model.* **43**, 22–35 (2012)
43. Ma, G., Kirby, J.T., Hsu, T.J., Shi, F.: A two-layer granular landslide model for tsunami wave generation: theory and computation. *Ocean Model.* **93**, 40–55 (2015)
44. Masson, D.G., Harbitz, C.B., Wynn, R.B., Pedersen, G., Lovholt, F.: Submarine landslides: processes, triggers and hazard prediction. *Philos. Trans. R. Soc. A* **364**, 2009–2039 (2006)
45. Mergili, M., Fischer, J.-T., Krenn, J., Pudasaini, S.P.: r.avaflow v1, an advanced open-source computational framework for the propagation and interaction of two-phase mass flows. *Geosci. Model Dev.* **10**(2), 553–569 (2017). <https://doi.org/10.5194/gmd-10-553-2017>
46. Mergili, M., Emmer, A., Juřicová, A., Cochachin, A., Fischer, J.-T., Huggel, C., Pudasaini, S.P.: How well can we simulate complex hydro-geomorphic process chains? The 2012 multi-lake outburst flood in the Santa Cruz Valley (Cordillera Blanca, Peru). *Earth Surf. Process. Landf.* **43**, 1373–1378 (2018a). <https://doi.org/10.1002/esp.4318>
47. Mergili, M., Frank, B., Fischer, J.-T., Huggel, C., Pudasaini, S.P.: Computational experiments on the 1962 and 1970 mass flow events at Nevado Huascarán (Peru) with r.avaflow: lessons learned for predictive mass flow simulations. *Geomorphology* **322**, 15–28 (2018)
48. Miao, H., Wang, G., Yin, K., Kamai, T., Li, Y.: Mechanism of the slow-moving landslides in Jurassic red-strata in the three gorges reservoir. *Eng. Geol.* (2014). <https://doi.org/10.1016/j.enggeo.2013.12.017>
49. Mohammed, F.: Physical modeling of tsunamis generated by three-dimensional deformable granular landslides, PhD Dissertation. Georgia Institute of Technology (2010)
50. Mohammed, F., Fritz, H.M.: Physical modeling of tsunamis generated by three-dimensional deformable granular landslides. *J. Geophys. Res.* **117**, 705–718 (2012). <https://doi.org/10.1029/2011JC007850>
51. Monaghan, J.J., Kos, A.: Scott Russell's wave generator. *Phys. Fluids* **12**, 622–630 (2000)
52. Nettleton, I.M., Martin, S., Hencher, S., Moore, R.: Debris flow types and mechanisms. In: Winter, M.G., McGregor, F., Shackman, L. (eds.) Scottish Road Network Landslides Study, pp. 45–67. The Scottish Executive, Edinburgh (2005)
53. Oetjen, J., Engel, M., Brückner, H., Pudasaini, S.P., Schütttrumpf, H.: Enhanced field observation based physical and numerical modeling of tsunami induced boulder transport: phase 1: physical experiments. *Coast. Eng. Proc.* (2017)
54. Naaim, M., Faug, T., Naaim, F., Eckert, N.: Return period calculation and passive structure design at the Taconnaz avalanche path, France. *Ann. Glaciol.* **51**(54), 89–97 (2010)
55. Petrakov, D.A., Tutubalina, O.V., Aleinikov, A.A., Chernomorets, S.S., Evans, S.G., Kidyaeva, V.M., Krylenko, I.N., Norin, S.V., Shakhmina, M.S., Seynova, I.B.: Monitoring of Bashkara Glacier Lakes (Central Caucasus, Russia) and modelling of their potential outburst. *Nat. Hazards* (2011). <https://doi.org/10.1007/s11069-011-9983-5>
56. Pitman, E.B., Le, L.: A two-fluid model for avalanche and debris flows. *Philos. Trans. R. Soc. A* **363**(3), 1573–1601 (2005)
57. Pudasaini, S.P., Hutter, K.: Rapid shear flows of dry granular masses down curved and twisted channels. *J. Fluid Mech.* **295**, 193–208 (2003)
58. Pudasaini, S.P., Wang, Y., Hutter, K.: Modelling debris flows down general channels. *Nat. Hazards Earth Syst. Sci.* **5**, 799–819 (2005)
59. Pudasaini, S.P., Hutter, K.: Avalanche Dynamics: Dynamics of Rapid Flows of Dense Granular Avalanches. Springer, Berlin (2007)
60. Pudasaini, S.P.: A general two-phase debris flow model. *J. Geophysics. Res.* **117**, F03010 (2012). <https://doi.org/10.1029/2011JF002186>
61. Pudasaini, S.P.: Dynamics of submarine debris flow and tsunami. *Acta Mech.* **225**, 2423–2434 (2014). <https://doi.org/10.1007/s00707-014-1126-0>
62. Pudasaini, S.P., Krautblatter, M.: A two-phase mechanical model for rock-ice avalanches. *J. Geophys. Res. Earth Surf.* (2014). <https://doi.org/10.1002/2014JF003183>
63. Qiao, C., Ou, G., Pan, H.: Numerical modelling of the long runout character of 2015 Shenzhen landslide with a general two-phase mass flow model. *Bull. Eng. Geol. Environ.* (2018). <https://doi.org/10.1007/s10064-018-1329-z>
64. Sammarco, P., Renzi, E.: Landslide tsunamis propagating along a plane beach. *J. Fluid Mech.* **598**, 107–119 (2008). <https://doi.org/10.1017/S0022112007009731>
65. Savage, S.B., Hutter, K.: The motion of a finite mass of granular material down a rough incline. *J. Fluid Mech.* **199**, 177–215 (1989)
66. Savage, S.B., Hutter, K.: Dynamics of avalanches of granular materials from initiation to runout. Part I: analysis. *Acta Mech.* **86**, 201–223 (1991)
67. Slingerl, R.L., Voight, B.: Occurrences, Properties, and Predictive Models of Landslide-generated Water Waves, pp. 317–397. Elsevier, Amsterdam (1979)
68. Takahashi, T.: Debris Flow. IAHR-AIRH Monograph Series A, Balkema, Rotterdam, Netherlands (1991)
69. Tai, Y.-C., Noelle, S., Gray, J.M.N.T., Hutter, K.: Shock-capturing and front-tracking methods for granular avalanches. *J. Comput. Phys.* **175**(1), 269–301 (2002)
70. Virotoulet, S., C'ebron, D., Kimoun, O., Kharif, C.: Shallow water waves generated by subaerial solid land-slides. *Geophys. J. Int.* **193**, 747–762 (2013). <https://doi.org/10.1093/gji/ggs133>
71. Virotoulet, S., Baker, J.L., Edwards, A.N., Johnson, C.G., Gjaltema, C., Clavel, P., Gray, J.M.N.T.: Multiple solutions for granular flow over a smooth two-dimensional bump. *J. Fluid Mech.* **815**, 77–116 (2017). <https://doi.org/10.1017/jfm.2017.41>
72. Vischer, D.L., Hager, W.H.: Dam Hydraulics, pp. 87–107. Wiley, Hoboken (1998)
73. Von Hardenberg, W.G.: Expecting disaster: the 1963 landslide of the Vajont Dam. *Environ. Soc. Portal Arcadia* **2011**, 8 (2011)
74. Walder, J.S., Watts, P., Sorensen, O.E., Janssen, K.: Tsunamis generated by subaerial mass flows. *J. Geophys. Res.* **108**(5), 2236–2255 (2003)
75. Ward, S.N., Day, S.: The 1963 landslide and flood at Vajont Reservoir Italy. A tsunami ball simulation. *Ital. J. Geosci.* **130**(1), 16–26 (2011). <https://doi.org/10.3301/IJG.2010.21>

76. Worni, R., Stoffel, M., Huggel, C., Volz, C., Casteller, A., Luckman, B.: Analysis and dynamic modeling of a moraine failure and glacier lake outburst flood at Ventisquero Negro, Patagonian Andes (Argentina). *J. Hydrol.* **444–445**, 134–145 (2012)
77. Yalciner, A.C., Pelinovsky, E., Okal, E., Synolakis, C.E.: *Submarine Landslides and Tsunamis*. Kluwer Academic Publishers, Dordrecht (2003)
78. Yavari-Ramshe, S., Ataie-Ashtiani, B.: Numerical modeling of subaerial and submarine landslide-generated tsunami waves—recent advances and future challenges. *Landslides* **13**(6), 1325–1368 (2016)
79. Zhai, J., Yuan, L., Liu, W., Zhang, X.: Solving the Savage–Hutter equations for granular avalanche flows with a second-order Godunov type method on GPU. *Int. J. Numer. Methods Fluids* **77**, 381–399 (2015). <https://doi.org/10.1002/fld.3988>

Publisher's Note Springer Nature remains neutral with regard to jurisdictional claims in published maps and institutional affiliations.